Contents lists available at ScienceDirect

International Journal of Engineering Science

journal homepage: www.elsevier.com/locate/ijengsci

A multiple-network poroelastic model for biological systems and application to subject-specific modelling of cerebral fluid transport

Liwei Guo [a,*], John C. Vardakis [a,1], Dean Chou [b], Yiannis Ventikos [a,*]

[a] Department of Mechanical Engineering, University College London, United Kingdom
[b] Department of Mechanical Engineering, National Central University, Taoyuan County, Taiwan

ARTICLE INFO

ABSTRACT

Biological tissue can be viewed as porous, permeable and deformable media infiltrated by fluids, such as blood and interstitial fluid. A finite element model has been developed based on the multiple-network poroelastic theory to investigate transport phenomenon in such biological systems. The governing equations and boundary conditions are adapted for the cerebral environment as an example. The numerical model is verified against analytical solutions of classical consolidation problems and validated using experimental data of infusion tests. It is then applied to three-dimensional subject-specific modelling of brain, including anatomically realistic geometry, personalised permeability map and arterial blood supply to the brain. Numerical results of smoking and non-smoking subjects show hypoperfusion in the brains of smoking subjects, which also demonstrate that the numerical model is capable of capturing spatio-temporal fluid transport in biological systems across different scales.

1. Introduction

Poroelastic theory is widely used in civil, petroleum and biomedical engineering. Two directions are commonly acknowledged for the development of the poroelastic theory (Coussy, Dormieux & Detournay, 1998; de Boer, 1992): one is based on mixture theory while the other one is founded on macroscale theories, mainly represented by the work of Biot. Mixture theory owes much of its current structure to the early works of Truesdell (1957a, 1957b, 1962). Extensive reviews of the literature on mixture theory can be found in the papers by Atkin and Craine (1976a), Bowen (1976) and Bedford and Drumheller (1983), and the books by Samohyl (1987) and Rajagopal and Tao (1995), Truesdell (1984). Mixture theory assumes that the domain of a mixture can be viewed as a superposition of several single interpenetrating continua, each representing a different constituent and following its own motion; at any time, each position in the mixture domain is occupied simultaneously by one particle from each constituent, in a homogenised sense (Atkin & Craine, 1976a). Based on mixture theory, the governing equations for poroelasticity are derived through averaging procedures, generally using a Eulerian description.

---

* Corresponding authors.
  E-mail addresses: liwei.guo@ucl.ac.uk (L. Guo), y.ventikos@ucl.ac.uk (Y. Ventikos).
[1] Present address: Centre for Computational Imaging & Simulation Technologies in Biomedicine (CISTIB), School of Computing, University of Leeds, United Kingdom.

a. Single-porosity/single-permeability.   b. Dual-porosity/dual-permeability.
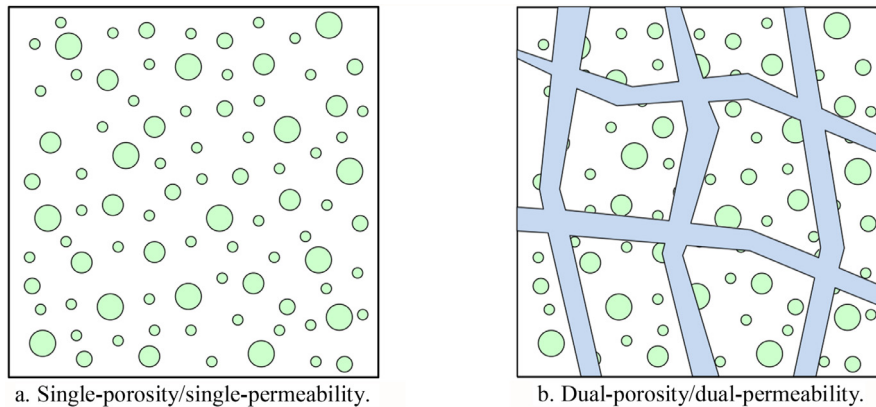
Fig. 1. Schematic illustration of two types of naturally fractured reservoirs. (a) Only matrix pores exist in the system, which has one porosity and one permeability. (b) Both fissures and matrix pores exist; each has its own porosity and permeability.

In contrast to mixture theory, the macroscale theories (e.g. Biot's consolidation theory) assume that the stress and other related variables hold at the macroscale, as well as most of the classical field equations of continuum mechanics, generally using a Lagrangian description (Coussy et al., 1998). It has been demonstrated that the Biot's theory is a special case of the more general formulation derived within the content of mixture theory, when appropriate assumptions are made (Bowen, 1982; Rajagopal, 2007; Rajagopal & Tao, 1992, 2005). The coefficients used in these two groups of theories also have different physical interpretations (Schanz & Diebels, 2003).

Based on mixture theory, the governing equations for poroelasticity are derived on a strict mathematical ground. For example, the Darcy's equations in a generalised form can be deduced from mixture theory (Atkin & Craine, 1976b; Kannan & Rajagopal, 2008; Munaf, Lee, Wineman & Rajagopal, 1993), whereas they were assumed in Biot's work as an approximation of the balance of linear momentum for the fluid that is flowing through a porous solid (Rajagopal, Saccomandi & Vergori, 2010; Subramanian & Rajagopal, 2007). However, the Biot theory – a heuristic model, provides a straightforward continuum theory for materials with microstructures and leads to satisfactory results in describing porous media models (de Boer et al., 1988; Rohan & Lukeš, 2017). One of the main advantages is that the constitutive relationships involve well defined and measurable quantities at the macroscale, such as the increment of fluid content, which makes it more tractable for engineering applications (Coussy et al., 1998).

The consolidation theory describing a porous medium at the macroscale was proposed by Biot (1941) and then further developed by Biot (1955, 1956) and other researchers (Prevost, 1980; Thigpen & Berryman, 1985; Zienkiewicz, Chan, Pastor, Paul & Shiomi, 1990; Zienkiewicz & Shiomi, 1984). A traditional engineering field to apply the poroelastic theory is soil and rock mechanical problems in geological systems, where it is mainly used to understand subsidence, estimate hydrocarbon volumes, and predict stresses around boreholes (Wang, 2000). For complicated engineering applications, the finite element method is often used to solve poroelastic problems. Its application to poroelasticity began in 1969 (Sandhu & Wilson, 1969) on a special case of incompressible fluid and solid constituents in soil. Since then numerous research activities have been devoted in applying various spatial and temporal discretisation schemes and in the investigations of numerical characteristics, e.g. stability, convergence and error estimation, of existing algorithms. Some examples are the work of Vermeer and Verruijt (1981) to investigate the numerical instability at early stages of consolidation, the work of Wheeler and Gai (2007), which used mixed finite element spaces for pore pressure and continuous Galerkin methods for displacements, and that of Ferronato, Castelletto and Gambolati (2010), which used the lowest order Raviart-Thomas mixed space for the fluid pore pressure and flux, and linear tetrahedral elements for the displacement.

A more complicated poroelastic theory considers the multi-porous nature of geological systems, i.e. characterised by several distinct families of diffusion or flow paths (Wilson & Aifantis, 1982). To capture diffusion or infiltration processes in such media, the multiple-network poroelastic theory (MPET) was developed from the classical form of Biot's consolidation theory (Biot, 1941; Detournay & Cheng, 1993), which describes an isotropic and nearly incompressible solid matrix and homogeneous porous medium. This concept of multiple-porosity was first introduced by Aifantis (1977) and then developed and used for geomaterials (Aifantis, 1979; Aifantis & Hill, 1980; Bai, 1999, 1993; Berryman & Wang, 1995; Choo & Borja, 2015; Kim, Sonnenthal & Rutqvist, 2012; Mehrabian & Abousleiman, 2014), where fissured rocks or aggregated soils exhibit more than one scale in terms of fluid flow and solid deformation. One example is shown in Fig. 1, which compares two types of porous media representing naturally fractured reservoirs – the one on the left-hand side has only matrix pores and the other one has both matrix pores and fissures. In the latter case, the connected fissure network provides conduits for fluid flow, which can be more dominant, compared with the generally low permeability of the rock matrix. Therefore, for such a medium with discrete fractions of varying solid compressibilities and permeabilities, a multiple-porosity/multiple-permeability model appears more appropriate to represent the realistic system (Bai et al., 1993).

Porous structures also exist in many biological systems. One example is biological tissue, such as brain, kidney and bone. Regardless of the specific and distinctive nature of the microstructures within the tissue, from a mechanical point of view,

they can all be viewed as porous, permeable and deformable media. However, many adaptions need to be made in order to use the poroelastic theory in the field of biomechanical problems, which can be understood by comparing the differences between geological and biological systems.

The first main difference is the mechanical response. For porous materials, the mechanical response mainly depends on two aspects: microstructural characteristics and mechanical properties of individual constituents (Thigpen & Berryman, 1985). Although the mechanical properties of individual constituents (e.g. constitutive relationships for solid skeletons) may not be fundamentally different, the microstructures of geomaterials are characterised by size, shape, orientation and distribution of grains, pores and cracks, etc. However, the biological systems have completely different microstructures, such as Aquaporin-4 in the glial cell membrane in the brain, which makes the membrane permeable to water by functioning as water channels (Abbott, Rönnbäck & Hansson, 2006; Preston, Carroll, Guggino & Agre, 1992). The second main difference is the focus of mechanical analysis. The analysis of geological systems greatly focuses on stress and deformation, which provide important criteria to determine the state of the structure, e.g. failure. For biological materials, however, the mechanical analysis should pursue a broader scope due to the inherent complexity; such examples are remodelling processes and transport phenomena. The reason to emphasise transport phenomena in biological systems is that they play important roles in the supply of nutrients and drainage of waste products, which are essential to maintain the function of a biological system (Xie et al., 2013).

Taking these differences into account, attention needs to be paid to make adjustments when using the poroelastic theory for biological systems. By analogy it can be known that although there are no discrete fracture networks, a hierarchical system of blood vessels, i.e. the vascular tree, exits in biological systems. The vascular tree and the fracture network are similar in the sense that they both provide flow paths in porous media, i.e. high porosity and high permeability networks. More specifically, the vascular tree consists of large arterial vessels from which smaller vessels bifurcate and diverge into capillaries, and then the capillaries assemble and converge into venous vessels. In addition to the blood flow, there is also interstitial fluid, which is a thin layer of liquid surrounding tissue cells in the body and can be considered as flow through a low porosity and low permeability network. In terms of the coupling between fluid and solid, it is known that tissue deformation can cause changes in blood perfusion (i.e. fluid filtration) (Hoffman & Spaan, 1990). Therefore, the multiple-porosity/multiple-permeability concept is suitable for biological systems as well, where the solid matrices and multiple fluid compartments are considered to be separate and completely overlapping continua (Bai et al., 1993). Blood flow in the vascular tree can be described by the communication between fluid compartments (Vankan, Huyghe, Janssen & Huson, 1996), such as flux from the arterial compartment to the arteriole/capillary compartment and further into the venous compartment.

Due to the inherent complexity of biological systems, numerical methods are often necessary to obtain accurate solutions in a timely manner. In the field of computational biomechanics, many software suites have been developed for mechanistic modelling, such as SfePy (Rohan & Cimrman, 2012), FEBio (Maas, Ellis, Ateshian & Weiss, 2012), FEniCS (Logg, Mardal & Wells, 2012) and others (Chen et al., 2018; Paulsen et al., 1999). However, they have not been used to apply a multiple-porosity/multiple-permeability model on anatomically accurate three-dimensional geometries. In terms of more customised poroelastic theory, numerical models have been used successfully in the modelling of biomechanical processes, e.g. hydrocephalus, using either one fluid network (Kaczmarek et al. 1997; Sivaloganathan, Stastna, Tenti & Drake, 2005; Smillie, Sobey & Molnar, 2005; Tully & Ventikos, 2009; Wirth & Sobey, 2006) or more than one fluid networks (Levine, 2000, 2008; Sobey, Eisentrager, Wirth & Czosnyka, 2012; Tully & Ventikos, 2011). However, the problem with these models is that they are limited to simplified brain geometries. For example, in simplified one-dimensional models, the spatial variation was reduced to a solution field along a line (Kaczmarek et al. 1997; Levine, 2000, 2008; Sivaloganathan et al., 2005; Smillie et al., 2005; Sobey et al., 2012; Tully & Ventikos, 2009, 2011); and even in three-dimensional models, the cortical surface was simplified into a sphere and the amalgamated ventricles were in the form of simplified geometry (e.g. ellipsoid) (Wirth & Sobey, 2006).

The objective of this paper is to present a newly developed finite element model of the multiple-network poroelastic theory for biological systems and application to three-dimensional subject-specific modelling of cerebral fluid transport that features anatomically realistic geometry and personalised parameters and boundary conditions. The paper is organised in the following way. Firstly in Section 2, a general description is given on the multiple-network poroelastic theory in the context of biological systems. The emphasis here is to introduce the physical concepts, and the detailed mathematical model, including governing equations and boundary conditions in a cerebral environment, are given in Section 3. In addition to the mathematical model, Section 3 also provides details of the numerical implementation of the in-house finite element model. Next, in Section 4 the numerical model is verified against the analytical solutions of the Terzaghi's problem and the Mandel's problem. It is also validated against experimental data from infusion tests on mouse brain in Section 5. Section 6 presents the numerical results of applying the numerical model on subject-specific modelling, where the results are compared between a smoker and a non-smoker. Lastly, Section 7 discusses the limitations of the current model and provides suggestions for future work, and Section 8 draws some conclusions.

2. Multiple-network poroelastic theory in biological systems

To adapt the classical multiple-network poroelastic theory to the modelling of biomechanical processes in biological systems, it was proposed to treat the biological tissue as a permeable and deformable solid matrix, and various blood networks and interstitial fluid etc. as fluid networks (Tully & Ventikos, 2011). Within such an *n*-MPET system, the solid
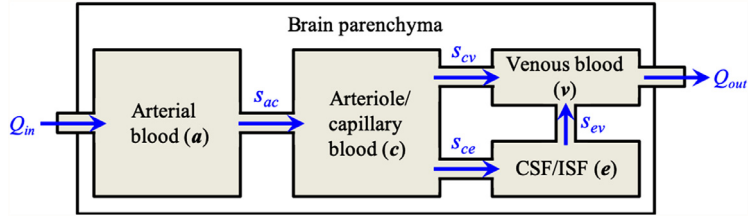
Fig. 2. The 4-MPET model for the cerebral environment. Flow is prohibited between the CSF/ISF and the arterial blood network, while directional transfer exists between (*a*) and (*c*), (*c*) and (*v*), (*c*) and (*e*) and finally (*e*) and (*v*).

matrix (biological tissue) is permeated by $i = 1, 2, 3, \ldots, n$ different fluid networks – each having a unique porosity (ϕ_i), density (ρ_i), permeability (k_i), pressure (p_i), filtration velocity (Darcy velocity) (v_i) and increment of fluid content (ζ_i).

In the cerebral environment, which is the application this paper aims at, the multiple-network poroelastic model can by illustrated by Fig. 2. The 4-MPET (four-network poroelastic theory) model was proposed to conduct mechanistic modelling of fluid transport through the brain parenchyma (Tully & Ventikos, 2011). Biologically, in a porous medium representing the cerebral environment, the solid matrix represents the brain parenchyma, and the communicating fluid phases considered are: an arterial network (*a*), an arteriole/capillary network (*c*), a cerebrospinal fluid/interstitial fluid (CSF/ISF) network (*e*) and a venous network (*v*) (Fig. 2). The separation of arterial and arteriole networks is based on the consideration of wildly different resistances between large and small arteries. Similar consideration was adopted in the modelling of coronary blood flow in the heart (Lee & Smith, 2012; Smith, Pullan & Hunter, 2002), where the arterial tree consists of several compartments. In general, arterioles are defined as the primary resistance vessels that enter an organ to distribute arterial blood into capillary beds, which provides more than 80% of the resistance to blood flow in the body (Christensen & Mulvany, 2001; Martinez-Lemus, 2011; Mulvany & Aalkjaer, 1990). Therefore the arterial blood is further segmented into a high pressure arterial network and a lower pressure arteriole/capillary network (Tully & Ventikos, 2011).

This model allows for the simultaneous solutions of continuity and momentum conservation equations, in four interconnected fluid compartments, within a deformable solid matrix (parenchymal tissue). In this paper, this 4-MPET model is chosen as the theoretical template for the development of the finite element model.

3. Finite element model

3.1. Governing equations

The formulation of the MPET theory comprises three components: a mechanical equilibrium equation governing elastic deformation; Darcy's equations for modelling fluid flow; and a mass conservation expression. The governing equations use the parenchymal tissue displacement (**u**) and the pore pressures of the fluid networks p_i as the primitive variables. The general formulations are listed below.

$$G\nabla^2\mathbf{u} + (G+\lambda)\nabla\varepsilon = \sum \alpha_i \nabla p_i \tag{1}$$

$$S_i \frac{\partial p_i}{\partial t} + \sum S_{ij} \frac{\partial p_j}{\partial t} + \alpha_i \frac{\partial \varepsilon}{\partial t} = \frac{\mathbf{k}_i}{\mu_i} \nabla^2 p_i + \sum s_{ji} \tag{2}$$

Eq. (1) is the equilibrium equation, which describes the momentum balance in the porous medium. Here, **u** is the displacement vector; p_i the scalar pore pressure in each fluid compartment ($i = a, c, e, v$); G the shear modulus; λ the Lamé's constant; ε the dilatational strain; α_i the Biot–Willis coefficient for each fluid compartment which satisfies $\phi \leq \alpha_a + \alpha_c + \alpha_e + \alpha_v \leq 1$ (Berryman, 1992; Wang, 2000), where ϕ is the total porosity. Body forces on the bulk material, such as gravity, are neglected in Eq. (1). It should be noted that the acceleration frequencies are low in biological flows, so the inertia terms are neglected in the governing equations (Chou, Vardakis, Guo, Tully & Ventikos, 2016; Tully & Ventikos, 2011).

Eq. (2) is the continuity equation, which describes the mass balance. Here, S_i is the specific storage (a measure of the released fluid volume per unit pressure in the control volume at constant strain for each fluid compartment); S_{ij} ($i \neq j$) is the coupling term describing the effect of excess pore pressure of fluid compartment j on the fluid content increment of another fluid compartment i; $\mathbf{k}_i$ is the permeability tensor for each of the four fluid compartments, which reduces to $\mathbf{k}_i = k_i\mathbf{I}$, with k_i a constant and **I** the unit tensor, for an isotropic medium; and μ_i is the viscosity of each fluid. The s_{ji} terms on the right-hand side of Eq. (2) define spatially varying source $s_{ji} > 0$) or sink ($s_{ji} < 0$) densities (rate of fluid transfer between networks) (Tully & Ventikos, 2011; Vardakis, Tully & Ventikos, 2013).

It should be noted that the cross-porosity storage effect (S_{ij}), which means the microscopic coupling effect between the volumetric deformation of different pore systems (Khalili, 2003), is not considered in this paper. In engineering applications, this effect can be considered (Mehrabian & Abousleiman, 2014) or neglected (Bai, Meng, Elsworth, Abousleiman & Roegiers, 1999) based on the specific assumptions adopted. In this paper, the cross-porosity storage effect is not considered mainly

due to the lack of experimental data to quantify the coupling terms in a physiological sense (Vardakis, Chou, Guo, Tully & Ventikos, 2017). Therefore, the specific formulations of the governing equations for a 4-MPET model presented in this paper are:

$$G\nabla^2\mathbf{u} + (G+\lambda)\nabla\varepsilon = \alpha_a\nabla p_a + \alpha_c\nabla p_c + \alpha_e\nabla p_e + \alpha_v\nabla p_v \tag{3}$$

$$S_a\frac{\partial p_a}{\partial t} + \alpha_a\frac{\partial\varepsilon}{\partial t} = \frac{\mathbf{k}_a}{\mu_a}\nabla^2 p_a + s_{ca} \tag{4}$$

$$S_c\frac{\partial p_c}{\partial t} + \alpha_c\frac{\partial\varepsilon}{\partial t} = \frac{\mathbf{k}_c}{\mu_c}\nabla^2 p_c + (s_{ac} + s_{ec} + s_{vc}) \tag{5}$$

$$S_e\frac{\partial p_e}{\partial t} + \alpha_e\frac{\partial\varepsilon}{\partial t} = \frac{\mathbf{k}_e}{\mu_e}\nabla^2 p_e + (s_{ce} + s_{ve}) \tag{6}$$

$$S_v\frac{\partial p_v}{\partial t} + \alpha_v\frac{\partial\varepsilon}{\partial t} = \frac{\mathbf{k}_v}{\mu_v}\nabla^2 p_v + (s_{cv} + s_{ev}) \tag{7}$$

The transfer between fluid networks is considered to be driven by a hydrostatic pressure gradient of the form, $s_{ji} = \omega_{ji}(p_j - p_i)$, where ω_{ji} is the transfer coefficient scaling the flow from network j to network i. The fluid flow between networks is derived from physiological considerations (Tully & Ventikos, 2011) and required to obey the law of continuity for the entire domain; hence, directionality between fluid compartments must be accurately specified. These are listed as follows:

1. Directional fluid transport always occurs from the arterial network (a) to the arteriole/capillary network (c):

$$s_{ac} = -s_{ca} = |s_{ac}| \geq 0 \tag{8}$$

2. Fluid transport from the arteriole/capillary network enters the CSF/ISF network (e) or the venous network (v):

$$s_{ce} = -s_{ec} = |s_{ce}| \geq 0 \tag{9}$$

$$s_{cv} = -s_{vc} = |s_{cv}| \geq 0 \tag{10}$$

3. The cerebrospinal fluid (CSF) flows into the venous compartment (v):

$$s_{ev} = -s_{ve} = |s_{ev}| \geq 0 \tag{11}$$

Compared with the general framework of mixture theory, the main assumptions and approximations used in the 4-MPET model are summarised as follows:

1. Body forces on the bulk material are neglected.
2. The inertia terms are neglected in the momentum balance equation.
3. Darcy's equations are used for fluid flow through a porous medium.
4. The pressure gradients are low in biological systems.
5. The fluid viscosity is constant.
6. The perfused tissue undergoes small deformations.
7. The transfer between fluid networks is driven by a hydrostatic pressure gradient.

3.2. Boundary conditions

A serious difficulty associated with solving boundary value problems within the context of mixture theory is the specification of appropriate boundary conditions (Tao & Rajagopal, 1993) as the assignment of boundary conditions to overlapping continua is not usually straightforward (Rajagopal, Yalamanchili & Wineman, 1994). For example, if traction boundary conditions are involved, then the difficulty is how to prescribe individual partial tractions when only the total traction is known. A method for overcoming this difficulty for some special mixtures has been provided by Rajagopal, Wineman and Gandhi (1986). In this paper, the boundary conditions are mainly defined from physiological considerations. The cerebral environment itself is complicated; therefore, assumptions and simplifications are introduced to implement boundary conditions for numerical modelling, which are discussed in detail in the rest of this section. Interpreting the boundary conditions in a physiological sense also makes the partition of boundary conditions between different fluid networks less complicated. Another factor that needs to be taken into account is the availability of data – either *in vivo* measurements or *in vitro* experiments, which are necessary to make the modelling results clinically relevant. Based on the considerations mentioned above, a set of boundary conditions applicable for the human brain has been derived for the 4-MPET model.

There are two boundary surfaces to define the volumetric domain that represents the brain parenchyma; the outer boundary is the cortical surface and the inner boundary is the ventricular wall (Fig. 3). Both surfaces are closed, and the cavity enclosed by the ventricular wall lies entirely within the cortical surface, i.e. no overlapping or penetration. The volumetric domain used in modelling is the space between these two surfaces. The boundary conditions for both the solid and fluid phases are listed in Table 1.
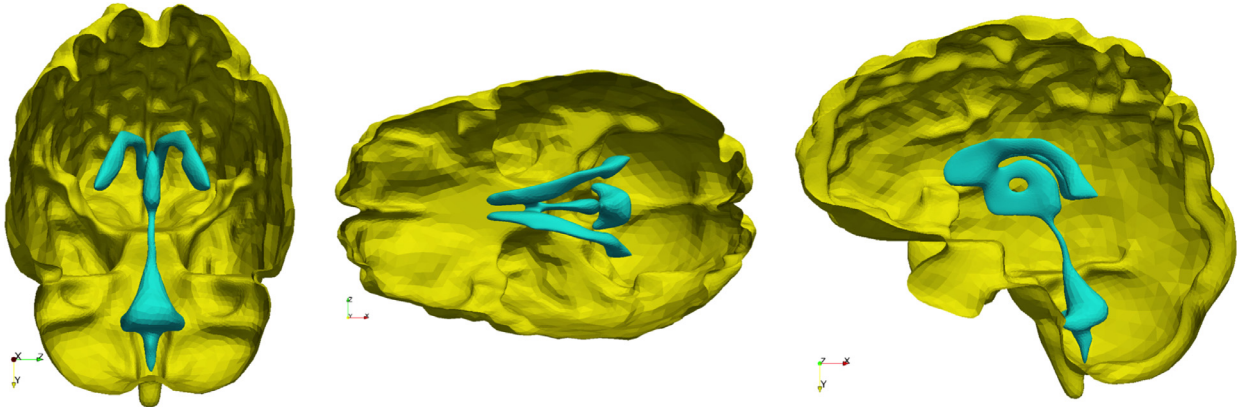
Fig. 3. The two boundary surfaces defining a typical simulated volumetric domain (brain parenchyma). The outer surface (yellow) represents the cortical surface and the inner surface (turquoise) represents the ventricular wall. It should be noted that it is a cavity inside the ventricular wall, i.e. not included in the modelling. (For interpretation of the references to color in this figure legend, the reader is referred to the web version of this article.)

Table 1
Boundary conditions used for the 4-MPET model.

	Cortical surface		Ventricular wall	
Displacement	$\mathbf{u} = 0$	(12)	*No displacement constraints*	
Arterial blood	$\nabla p_a \mathbf{n} = Q_a$	(13)	$\nabla p_a \mathbf{n} = 0$	(14)
Arteriole/capillary blood	$\nabla p_c \mathbf{n} = 0$	(15)	$\kappa_{c \to vent} \nabla p_c \mathbf{n} = -Q_p$	(16)
CSF/ISF	$p_e = p_v + \mu_e R Q_0$	(17)	$Q_p = \dfrac{\pi d^4}{128 \mu_e L}\left(p_e - p_e^{skull}\right)$	
			$\qquad - \dfrac{4\pi k_e}{\mu_e}\left(r_1 + u_1^n\right)^2 \nabla p_e \mathbf{n}$	
			$\qquad + 4\pi \left(r_1 + u_1^n\right)^2 \dot{u}$	(18)
Venous blood	$p_v = p_{bp}$	(19)	$\nabla p_v \mathbf{n} = 0$	(20)

The skull is assumed rigid to represent adult cases (Smillie et al., 2005). Previous research showed a compliant behaviour of the subarachnoid space, although the estimated deformations were small due to the large parenchyma surface area (Gupta, Soellinger, Boesiger, Poulikakos & Kurtcuoglu, 2009, 2010). In this paper, the CSF flow and mechanical response in the subarachnoid space is not considered; for simplicity, the rigid boundary condition is applied directly to the cortical surface, which assumes no displacement is allowed at this boundary (Eq. (12)). There are no displacement constraints at the ventricular wall, so it can expand or contract freely. For continuity of stresses, the pressure exerted by the CSF within the ventricles on the inner ependymal surface must balance the poroelastic stress in the parenchymal tissue (Tully & Ventikos, 2011; Vardakis et al., 2013, 2016), which is applied as a pressure boundary condition in the numerical modelling.

The arterial blood supply to the brain is mainly provided by two pairs of arteries – internal carotid arteries and vertebral arteries (Tortora & Derrickson, 2009). Due to the lack of explicit characterisation of vasculature in the 4-MPET model, the arterial blood supply to the brain is simplified into a flux boundary condition (Neumann boundary condition) Q_a at the cortical surface (Eq. (13)). More details about assigning the boundary condition for the arterial blood compartment is given in Section 6.

For the arteriole/capillary blood compartment, the production of CSF from the blood results in a pressure drop in the arteriole/capillary blood (Eq. (16)), where $\kappa_{c \to vent}$ is the resistance of the flow from the capillary network to the ventricles (through the choroid plexus), and Q_p is the rate of CSF production. Two assumptions are adopted in this boundary condition. First, there is no separation of the two extracellular fluid compartments in the brain – the cerebrospinal fluid (CSF) and the interstitial fluid (ISF) in the 4-MPET model, which assumes that all of the CSF/ISF is produced within the ventricles from blood at a production rate Q_p. However, it has been reported that approximately 20% of CSF in the human brain originates from brain ISF (Edsbagge, Tisell, Jacobsson & Wikkelso, 2004; Lei, Han, Yuan, Javeed & Zhao, 2017). In the current 4-MPET model, this part of CSF production is implicitly embedded in the combined CSF/ISF compartment. Second, the main site of CSF production in the ventricles is the choroid plexus, which is a highly vascularised tissue located within each ventricle of the brain and develops from several locations along the dorsal axis of the neural tube (Lun, Monuki & Lehtinen, 2015). The classical hypothesis involves the production of CSF at the choroid plexus of the lateral, third and fourth ventricles. However, it is still speculative as to the exact proportions of CSF production in the various choroid plexus sites (Gupta et al., 2009;

Vardakis et al., 2013). The 4-MPET model simplifies the production of CSF as a uniform distribution on the entire ventricular wall, instead of at specific locations. This simplification is also consistent with the homogenisation assumption adopted for the 4-MPET model.

The CSF/ISF compartment has a Dirichlet boundary condition at the cortical surface and a mixed boundary condition at the ventricular wall. At the cortical surface, the boundary condition (Eq. (17)) represents the pressure rise resulted from the absorption of CSF into the venous network, where p_{bp} is the venous blood pressure at the cortical surface; μ_e is the viscosity of CSF; R is the resistance to outflow through the arachnoid granulations; and Q_0 is the out-flux of CSF at the skull (the rate of absorption Q_0 is assumed to be equal to the production rate Q_p in the quasi-steady approach). At the ventricular wall, the boundary condition (Eq. (18)) represents the conservation of the mass of fluid in the ventricles. Within the ventricles, it is assumed that any CSF that is produced (Q_p) and does not flow through the cerebral aqueduct (Poiseuille's law) or the parenchyma must accumulate within the ventricles, where d and L are the diameter and length of the cerebral aqueduct, respectively; r_1 is the distance from the centre to the ventricular wall; and u_1^n is the displacement at the ventricular wall.

3.3. Numerical implementation

The highly coupled governing equations of the MPET theory have been discretised using the finite element method and implemented into an in-house numerical code. First, for the equilibrium equation (Eq. (3)), the displacement field **u** is approximated in the continuous piecewise linear polynomial space,

$$\mathbf{u} = \begin{bmatrix} u \\ v \\ w \end{bmatrix} \simeq \begin{bmatrix} \sum_{i=1}^{n_n} N_i u_i \\ \sum_{i=1}^{n_n} N_i v_i \\ \sum_{i=1}^{n_n} N_i w_i \end{bmatrix} \tag{21}$$

where u, v and w are the displacement components in x, y and z-directions, respectively; N_i is the continuous piecewise linear polynomial ($i = 1, 2, \ldots, n_n$); n_n is the total number of nodes in the finite element mesh; and u_i, v_i and w_i are the nodal displacements in x, y and z-directions. Based on the principle of minimum potential energy, the algebraic form of the equilibrium equation is

$$\mathbf{Ku} - (\mathbf{Q}_a\mathbf{p}_a + \mathbf{Q}_c\mathbf{p}_c + \mathbf{Q}_e\mathbf{p}_e + \mathbf{Q}_v\mathbf{p}_v) = \mathbf{F} \tag{22}$$

where

$$\mathbf{K} = \int_{\Omega} \mathbf{B}^{\mathrm{T}}\mathbf{D}\mathbf{B}\mathrm{d}\Omega \tag{23}$$

$$\mathbf{Q}_i = \int_{\Omega} \alpha_i \mathbf{B}^{\mathrm{T}}\mathbf{h}\mathrm{d}\Omega \tag{24}$$

$$\mathbf{F} = \int_{\Omega} \mathbf{N}^{\mathrm{T}}\mathbf{b}\mathrm{d}\Omega + \int_{\Gamma_N} \mathbf{N}^{\mathrm{T}}\mathbf{t}_N\mathrm{d}\Gamma \tag{25}$$

K is the stiffness matrix with **B** the deformation matrix and **D** the elasticity matrix. $\mathbf{Q}_i$ is the load on the solid phase contributed from the ith fluid network and **h** is a mapping vector. **N** is the matrix of continuous piecewise linear polynomial functions (shape functions). **F** is the load vector with **b** the vector of body force in the three-dimensional domain Ω and $\mathbf{t}_N$ is the vector of external force at boundary Γ_N. The Dirichlet boundary conditions are imposed in a strong way.

For the continuity equations of the fluid networks (Eqs. (4)–(7)), the method of weighted residuals and the continuous Galerkin formulation are applied to derive the integral form (weak form) of these mass conservation equations. For example, the continuity equation of the ith fluid network can be written as,

$$\int_{\Omega} \left[\delta p_i \left(S_i \frac{\partial p_i}{\partial t} \right) + \nabla \delta p_i \frac{k_i}{\mu_i} \nabla p_i - \delta p_i s + \delta p_i \alpha_i \dot{\varepsilon} \right] \mathrm{d}\Omega - \int_{\Gamma_2} \delta p_i q_i \mathrm{d}\Gamma = 0 \tag{26}$$

where Ω is the three-dimensional domain; Γ_2 is the boundary where Neumann boundary condition is applied, and q_i is the flux prescribed in the Neumann boundary condition. The pore pressure of the ith fluid network in the MPET model p_i is approximated in the continuous piecewise linear polynomial space,

$$p_i \simeq \sum_{j=1}^{n_n} N_j p_j \tag{27}$$

where N_j is the continuous piecewise linear polynomial ($j = 1, 2, \ldots, n_n$); n_n is the total number of nodes in the mesh. Then the discretised continuity equation for one of the four fluid networks is

$$\mathbf{A}\dot{\mathbf{p}} + \mathbf{C}\mathbf{p} = \mathbf{P} \tag{28}$$

The elements in matrices **A, C** and vector **P** are

$$A_{ij} = S \int_{\Omega} N_i N_j \mathrm{d}\Omega \tag{29}$$

$$C_{ij} = \frac{k}{\mu} \int_{\Omega} \left(\frac{\partial N_i}{\partial x} \frac{\partial N_j}{\partial x} + \frac{\partial N_i}{\partial y} \frac{\partial N_j}{\partial y} + \frac{\partial N_i}{\partial z} \frac{\partial N_j}{\partial z} \right) \mathrm{d}\Omega \tag{30}$$

$$P_i = \int_{\Omega} s N_i \mathrm{d}\Omega - \alpha \int_{\Omega} \dot{\varepsilon} N_i \mathrm{d}\Omega + \int_{\Gamma_2} q N_i \mathrm{d}\Gamma \tag{31}$$

N_i and N_j are continuous piecewise linear polynomial functions at node i and j in the mesh, respectively. It can be seen from the right-hand side of Eq. (31) that the strain rate calculated from the displacement field acts as an additional source or sink term. The natural boundary condition, i.e. Neumann boundary condition, is applied at boundary Γ_2.

It is known that finite element solutions to consolidation problems may exhibit oscillation in the pressure field and locking when the permeability is very low, or at the very early stage in the consolidation process when small time-steps are used (Murad & Loula, 1994; Phillips & Wheeler, 2009; Vermeer & Verruijt, 1981; Yi, 2017; Zienkiewicz et al., 1990). This problem cannot be avoided without smoothing algorithms especially if the pressure and displacement fields are discretised by equal order elements (Choo & Borja, 2015; Reed, 1984). In this paper, the finite element model is developed for application in biological systems with effects taking place over long-term periods (such as chronic cases of hydrocephalus), where the focus is on steady-state responses, i.e. the early stage of consolidation is not important for using this model. For example, in the numerical application of Section 6, the numerical results at the very early stage of the simulation are disregarded and only the final states are considered in the analysis.

The temporal discretisation is conducted by using the method of weighted residuals. If the time-dependent pore pressure p is assumed to vary linearly between time t and $t+\Delta t$, the intermediate value can be estimated by

$$p = p_{n+1}\theta + p_n(1-\theta) \tag{32}$$

where p_n and p_{n+1} are the values of p at time t and $t+\Delta t$, respectively. θ is a scalar value between 0 and 1. The continuity equation can therefore be expressed as

$$(\mathbf{A}/\Delta t + \mathbf{C}\theta)\mathbf{p}_{n+1} + [\mathbf{C}(1-\theta) - \mathbf{A}/\Delta t]\mathbf{p}_n = \bar{\mathbf{P}} \tag{33}$$

where the right-hand side can be approximated using the same scheme,

$$\bar{\mathbf{P}} = \mathbf{P}_{n+1}\theta + \mathbf{P}_n(1-\theta) \tag{34}$$

In this paper, the time discretisation uses an implicit backward Euler scheme, i.e. $\theta = 1$. The discretised governing equations are solved by the standard KSP linear equation solver in the PETSc library (Balay et al., 2018a, 2018b).

In the present work, the discretised governing equations are solved sequentially in a tightly coupled manner, i.e. the pressure and displacement solutions are solved sequentially during a time-step until a convergence tolerance of 10^{-3} is reached. Previous comparisons showed that the iteratively coupled method and the fully coupled monolithic method gave the same accuracy if sufficiently tight convergence tolerance was used for iterations (Dean, Gai, Stone & Minkoff, 2006; Wheeler & Gai, 2007). The inner iterations within a time-step can be illustrated in Fig. 4. $\mathbf{p}_i^1$ is the initialised pore pressure of the ith fluid network at the first time-step and $\mathbf{p}_i^0$ is the initial condition of pore pressure. The current time-step is denoted by $n + 1$ and the previous time-step by n. ξ is an interpolation coefficient used on pressure solutions between inner iterations, which is chosen to be 0.9 in the current numerical code ($0 < \xi < 1$).

In the finite element formulation of the MPET model, the primitive variables are displacement and pore pressures of the fluid networks, i.e. a $p/\mathbf{u}$ formulation. Other variables of practical interests, such as Darcy velocity and increment of fluid content, can be derived from these primitive variables in the post-processing. For example, Darcy's equations are used to calculate Darcy velocities of the four fluid compartments.

$$\mathbf{v}_i = -\frac{\mathbf{k}_i}{\mu_i} \nabla p_i \tag{35}$$

where $\mathbf{v}_i$ is the Darcy velocity vector for each of the four fluid compartments ($i = a, c, e, v$), i.e. the volume of fluid crossing a unit area per unit time. The increment of fluid content ζ_i is defined as the variation of fluid volume per unit volume of porous material (Eq. (36)).

$$\zeta_i = \alpha_i \varepsilon + \frac{\alpha_i(1 - \alpha_i B_i)}{B_i K} p_i \tag{36}$$

where B_i is Skempton's coefficient of the ith fluid network and K is the bulk modulus. A positive ζ_i corresponds to a 'gain' of fluid by the porous medium. It should be noted that the accuracy of the Darcy velocity and the increment of fluid content depends on the accuracy of the pressure and displacement fields because they are not primitive variables in the formulation. An alternative way is to use a three-field formulation, where the Darcy velocity vector is a primitive variable, e.g. the work of Ferronato et al. (2010). However, it will increase the computational cost in terms of more degrees of freedom and longer computational time. Therefore, from a practical point of view, it is not necessary to include velocity in the discretised governing equations. Its accuracy can be accepted if the solutions of pressure and displacement are sufficiently accurate.
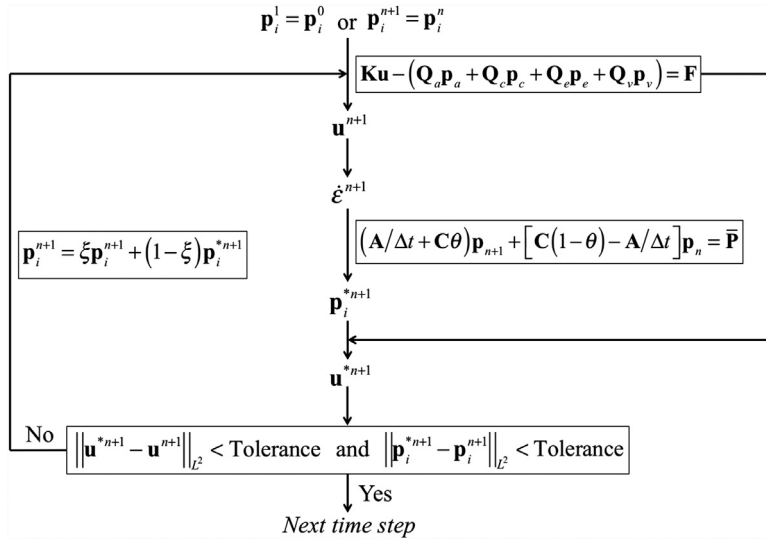
Fig. 4. Flowchart of inner iterations within each time-step. The variables with asterisk superscript are the updated values after each inner iteration.

Table 2
Material properties in the numerical verification tests.

Parameters	Values	Units
α	1.0	
λ	40	MPa
G	40	MPa
k/μ	1.02×10^{-9}	$m^2 Pa^{-1} s^{-1}$
S	1.65×10^{-4}	MPa^{-1}

4. Model verification

To ensure the formulation is consistent regardless of the number of fluid networks, an n-MPET model should give accurate results if reduced to a single-network poroelastic model (Berryman, 2002). In this section, the 4-MPET finite element model is reduced to one fluid compartment (i.e. n-MPET, $n = 1$), and verified against analytical solutions of two classical consolidation problems – the Terzaghi's problem (Terzaghi, 1925) and the Mandel's problem (Mandel, 1953).

4.1. Terzaghi's problem

The Terzaghi's problem (Terzaghi, 1925) describes the consolidation process of a finite layer. A constant stress is applied suddenly on the upper surface of a fluid-saturated layer (Fig. 5a). The only permeable boundary is where the load is applied, i.e. fluid can only drain from the upper surface. As the constant load continues, the sample keeps draining and gradually consolidates.

In numerical modelling, a column of length $L = 15$ m is used to represent the fluid-saturated finite layer; the cross-section is a 1 m $\times$ 1 m square. The column is discretised by 4-node tetrahedral elements with uniform size distribution; the average length of the element edge is $h = 0.5$ m. The positive z-direction is pointing downwards. Detailed mesh sensitivity tests have revealed that this mesh results in fully mesh independent solutions. For the solid phase, the only constraint is applied to the lower boundary ($z = 15$ m), where no displacement is allowed. For the fluid phase, non-permeable boundary conditions are applied to all the boundaries, except the upper surface ($z = 0$), where free drainage happens to maintain a constant pore pressure of zero.

The material used for this numerical test is assumed to be sand (Ferronato et al., 2010) and the material properties are given in Table 2. A time-step of $\Delta t = 0.1$ s is used in the modelling. The analytical solutions of Terzaghi's problem are given by Eqs. (37) and (38) (Ferronato et al., 2010; Wang & Hsu, 2009).

$$p(z,t) = \frac{4}{\pi} p_0 \sum_{m=0}^{\infty} \frac{1}{2m+1} \exp\left[\frac{-(2m+1)^2 \pi^2 ct}{4L^2}\right] \sin\left[\frac{(2m+1)\pi z}{2L}\right] \tag{37}$$

$$u(z,t) = c_M p_0 \left\{ (L-z) - \frac{8L}{\pi^2} \sum_{m=0}^{\infty} \frac{1}{(2m+1)^2} \exp\left[\frac{-(2m+1)^2 \pi^2 ct}{4L^2}\right] \cos\left[\frac{(2m+1)\pi z}{2L}\right] \right\} + u_0 \tag{38}$$
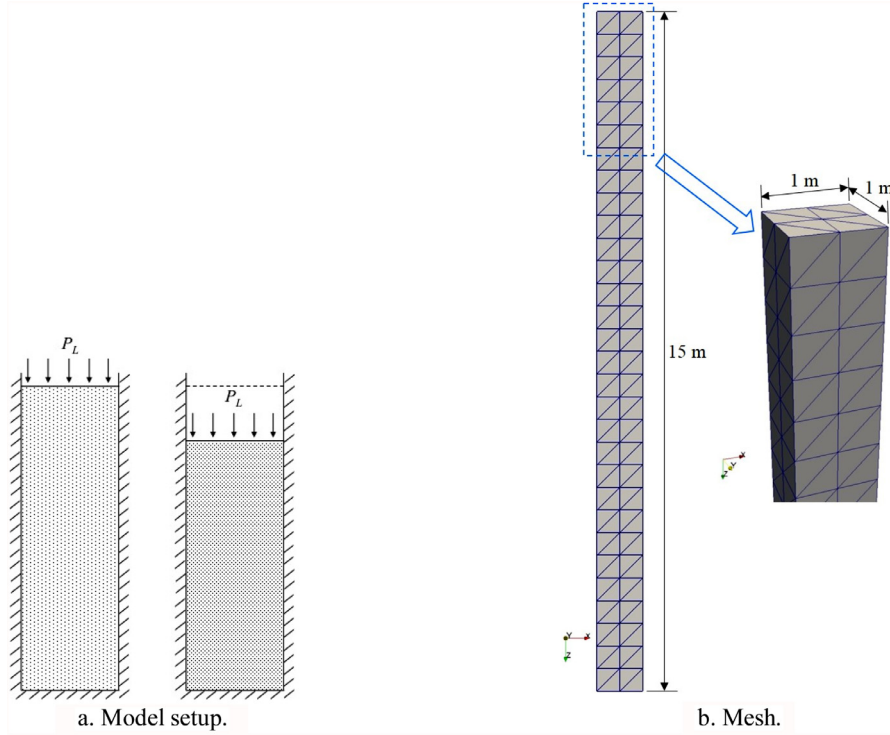
Fig. 5. Model setup and mesh for the modelling of the Terzaghi's problem.

where p is the pore pressure and u is the vertical displacement (positive downward). The consolidation coefficient c is defined as

$$c = \frac{k}{\mu\left(M^{-1} + \alpha^2 c_M\right)} \tag{39}$$

where c_M is the vertical uniaxial compressibility,

$$c_M = \frac{1}{\lambda + 2G} \tag{40}$$

and M is the Biot modulus,

$$M = \frac{1}{\phi\beta + (\alpha - \phi)c_{br}} \tag{41}$$

where ϕ is the porosity, β the fluid compressibility, and c_{br} the solid grain compressibility. It should be noted that for sand it is reasonable to assume that the sand grain is incompressible, which means $c_{br} = 0$. Therefore, the Biot modulus M can be expressed as

$$M = \frac{1}{\phi\beta} = \frac{1}{S} \tag{42}$$

where S is the specific storage coefficient defined in the governing equations.

In the analytical solutions, p_0 is the initial overpressure generated by the load applied instantaneously at time $t = 0$, given as
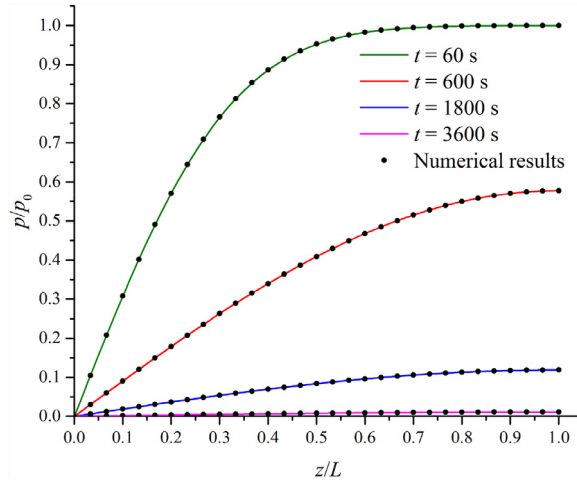
$$p_0(z) = \frac{\alpha M}{K_u + 4G/3}p_L \tag{43}$$
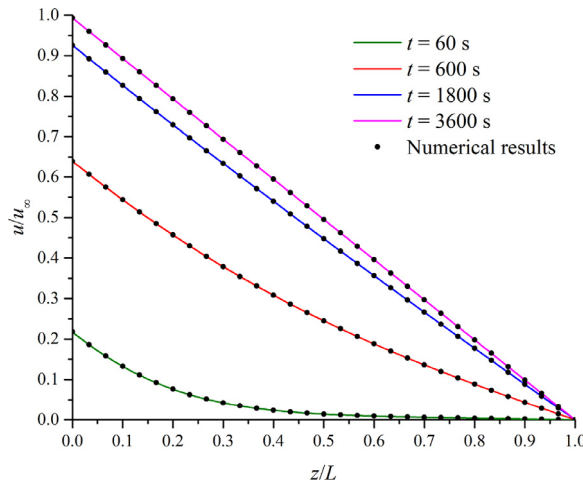
and an initial vertical displacement

$$u_0(z) = \frac{1}{K_u + 4G/3}p_L(L - z) \tag{44}$$

where K_u is the undrained bulk modulus, given by

$$K_u = \lambda + \frac{2G}{3} + \alpha^2 M \tag{45}$$

Fig. 6. Plots of the normalised pore pressure versus the normalised vertical distance in the numerical modelling of the Terzaghi's problem. The dots represent numerical results and the solid lines are analytical solutions.

Fig. 7. Plots of the normalised vertical displacement versus the normalised vertical distance in the numerical modelling of the Terzaghi's problem.

The constant load applied at the upper surface of the column ($z = 0$) is $P_L = 10^4$ Pa (Ferronato et al., 2010; Wang & Hsu, 2009).

The numerical results are compared and plotted with the analytical solutions in Figs. 6 and 7. It can be seen that both match the analytical solutions very well. It should be noted that the vertical displacement at the long time limit used for normalisation is (Wang, 2000)

$$u_\infty = \frac{P_L L}{\lambda + 2G} \tag{46}$$

which is the fully drained response at the upper surface $z = 0$.

4.2. Mandel's problem

The second test for verification is a simulation of the Mandel's problem, which describes a poroelastic medium compressed in one direction by two identical plates. The plates are assumed to be rigid, frictionless and impermeable. It can be seen from Fig. 8a that two constant loads are applied vertically on the plates. The fluid can only be drained from the two lateral surfaces, where there are no external forces.

In the numerical simulation, due to symmetry a cube with edge of 1 m is used to represent the poroelastic layer sandwiched between the plates (the shaded area in Fig. 8a). This cubic domain is discretised by 4-node tetrahedral elements, with an average edge of $h = 0.0625$ m. A time-step of $\Delta t = 0.01$ s is used in the modelling. The sample is assumed to be made of sand as well, the same as the one used in the Terzaghi's problem (Table 2).

The poroelastic layer in Mandel's problem is assumed to be infinitely long in the y-direction (the direction perpendicular to the paper), so it can be simplified into a two-dimensional plane strain problem (Fig. 8a), in which case the analytical
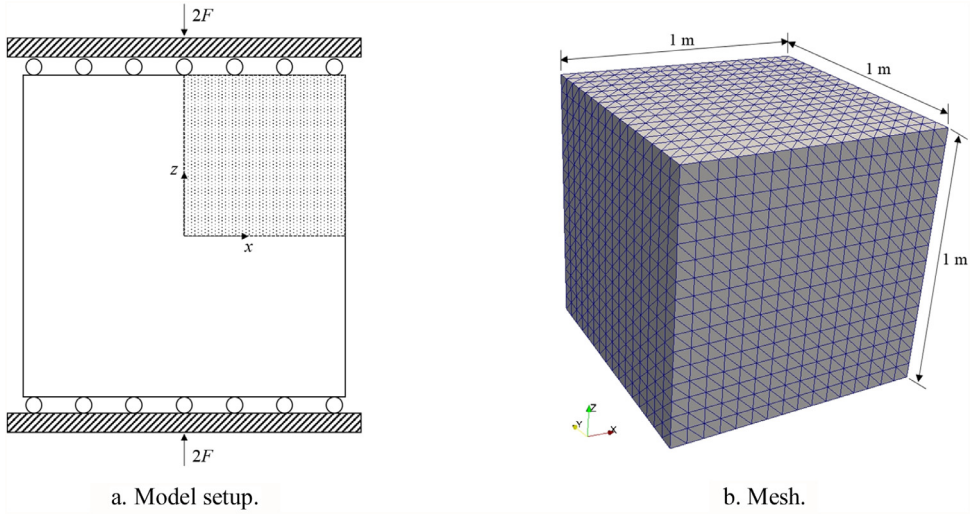
a. Model setup.   b. Mesh.

Fig. 8. Model setup and mesh for the modelling of the Mandel's problem.

solution for the pore pressure p is given by Ferronato et al. (2010):

$$p(x, t) = 2p_0 \sum_{n=1}^{\infty} \frac{\sin\alpha_n}{\alpha_n - \sin\alpha_n\cos\alpha_n} \left(\cos\frac{\alpha_n x}{a} - \cos\alpha_n \right) \exp\left(\frac{-\alpha_n^2 ct}{a^2} \right) \tag{47}$$

where α_n are the positive roots of the following equation

$$\tan\alpha_n = \frac{1 - \nu}{\nu_u - \nu}\alpha_n \tag{48}$$

In this analytical solution, c is the consolidation coefficient as defined in Eq. (39); a is the edge length of the cubic sample, $a = 1$ m; and p_0 is the initial overpressure generated by the loading suddenly applied to the plates at time $t = 0$,

$$p_0(x, z) = \frac{1}{3a}B(1 + \nu_u)F \tag{49}$$

where B is Skempton's coefficient, defined as

$$B = \frac{\alpha M}{K_u} \tag{50}$$

and ν_u is the undrained Poisson's ratio. It can be derived from the drained Poisson's ration ν by

$$\nu_u = \frac{3\nu + aB(1 - 2\nu)}{3 - \alpha B(1 - 2\nu)} \tag{51}$$

The load F in Eq. (49) is set to be $F = 10^4$ N/m.

Once again it can be seen that the numerical results are in very good agreement with the analytical solutions (Figs. 9 and 10). Importantly, the non-monotonic response of the pore pressure, i.e. the Mandel-Cryer effect (Cryer, 1963; Gibson, Gobert & Schiffman, 1990; Mandel, 1953; Schiffman, Chen & Jordan, 1969), has been accurately captured in the simulation (Fig. 10). At the very early stage, a uniform distribution of pore pressure is generated by the Skempton effect (Abousleiman, Cheng, Cui, Detournay & Roegiers, 1996; Skempton, 1954). As the consolidation progresses, the pore pressure near the lateral sides (x close to a) starts to decrease due to the drainage boundary conditions. In a poroelastic medium, both pore pressure and solid skeleton can contribute to the overall compressive stiffness. Therefore, the sample behaves in a more compliant manner at the lateral boundaries due to the reduction of pore pressure, while the central part of the domain (x close to 0) carries more compressive stress by the compatibility requirement, i.e. the compressive stress is transferred from the compliant region to the stiff region. The result is that the pore pressure continues to rise under this excessive compressive stress. In the long time limit, pore pressure will vanish everywhere in the domain.

4.3. Convergence analysis

The convergence of the 4-MPET finite element model was tested on a three-dimensional anatomically accurate geometry of human brain to investigate mesh independence and provide guidance on mesh resolution for subject-specific modelling. Twelve meshes were created from the same brain geometry, with total element numbers ranging from 104 075 to 8 688 950. All the simulations used the same set of parameters and boundary conditions. As it can be evidenced from Fig. 11, the
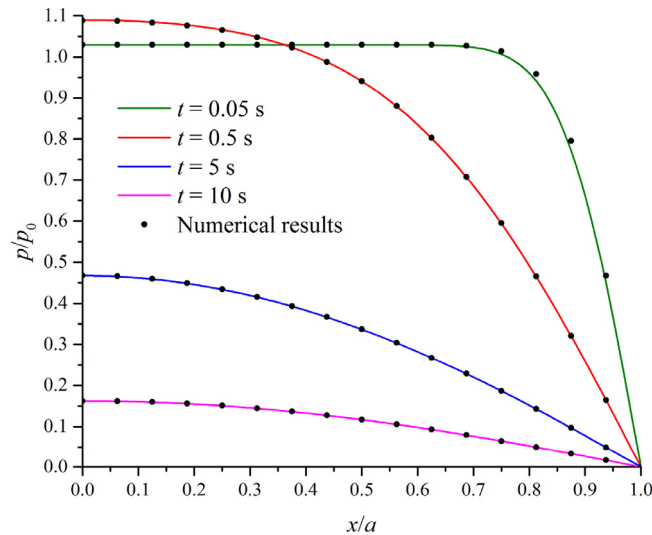
Fig. 9. Plots of the normalised pore pressure versus the normalised lateral distance in the numerical modelling of the Mandel's problem. The dots represent numerical results and the solid lines are analytical solutions.
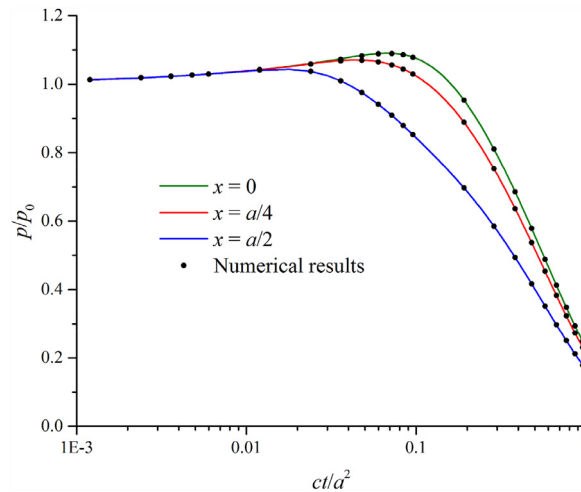

Fig. 10. Time histories of the normalised pore pressure in the numerical modelling of the Mandel's problem.

method exhibits good convergence characteristics and meshes of around two million tetrahedral elements are sufficient to capture salient features with good accuracy. Additional mesh independence testing results can be found in Guo et al. (2018), where plots of mean values in the entire parenchymal domain, as well as at selected representative positions, e.g. the white matter, the cortical surface and the ventricular wall, were given.

5. Model validation

In this section, the numerical model is validated against experimental data from infusion tests on six C57BL/6 J mouse brains (Vindedal et al., 2016), where the focus is on the circulation of the cerebrospinal fluid (CSF). The classical physiological theory believes that the CSF is produced in the choroid plexus and then flows through the cerebral ventricles and the subarachnoid space, until being reabsorbed into the bloodstream via arachnoid villi of the dural sinuses, along cranial nerve sheaths or through the nasal lymphatics (Abbott, 2004; Koh, Zakharov, & Johnston, 2005; Praetorius, 2007). Any breakdown in this circulation can cause serious consequences – one of them is communicating hydrocephalus, where obstacles exist in the cerebrospinal fluid (CSF) flow between the ventricular system and the subarachnoid space. In this case, infusion test is often used for the diagnosis because imaging alone is not sufficient to identify the obstacles (Boon et al., 2000; Juniewicz et al., 2005). In clinical practice, the most frequently used procedure is to inject CSF-like fluid (e.g. saline) into the subarachnoid space at a constant rate, usually via a lumbar puncture.
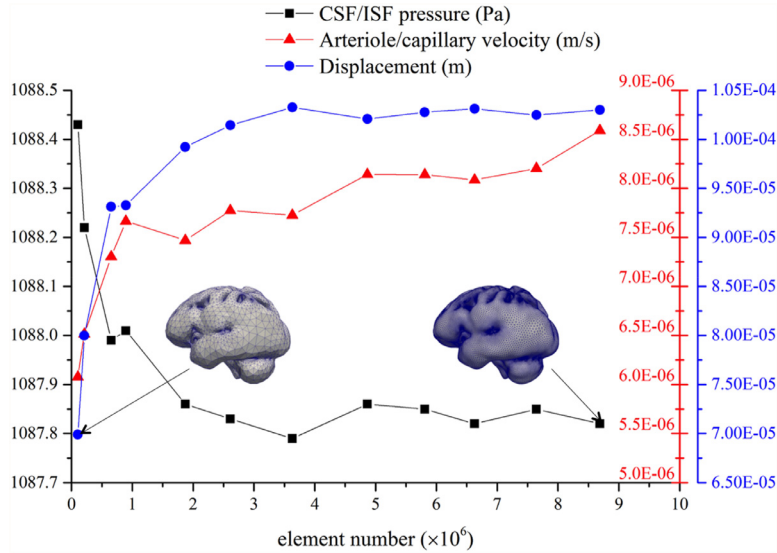
Fig. 11. Convergence plots of mesh independence tests. Mean values of the CSF/ISF pressure, Darcy velocity of the arteriole/capillary compartment and the displacement magnitude in the parenchymal domain are plotted against the number of tetrahedral elements (order of 10^6).

The infusion test has been simulated before either by mathematical modelling (Cieslicki, 2007) or poroelastic modelling (Sobey et al., 2012), but never using a highly physiologically specific multi-compartmental poroelastic model. During an infusion test, the injected CSF causes the intracranial pressure (ICP) to rise in order to accommodate the additional fluid, which also results in increased drainage. The ICP value recorded before infusion is called the baseline ICP. In the test, the ICP will reach a peak and then decline after the infusion is completed, but not return to the baseline value; this value is called post-infusion resting ICP. Two measurements are important here: The first one is the rate of rise to the peak providing an estimate of cerebral compliance and the second one is the difference between the baseline ICP and the peak value giving information about the resistance to CSF outflow (Andersson, Malm & Eklund, 2008). A mathematical model to describe such phenomenon was first proposed by Marmarou, Shulman and Rosende (1978) and later further developed by Avezaat and Eijndhoven (1984). The Marmarou model says that during an infusion test, the flow of CSF satisfies the following relationship according to the continuity requirement,

$$Q_P + Q_i = Q_R + Q_S \qquad (52)$$

where Q_P is the production of cerebrospinal fluid (CSF), Q_i the external infusion, Q_R the reabsorption, and Q_S the storage. In the numerical modelling of this section, the external infusion $Q_i = 2$ μl/min (over a period of five minutes), as previously described (Iliff et al., 2012) and it is the same value as the one used in the experiments (Vindedal et al., 2016). The value of CSF production is obtained from literature (Simon & Iliff, 2016), $Q_p = 0.35$ μl/min. The reabsorption of CSF happens at the cortical surface at a rate of

$$Q_R = \frac{p - p_{ss}}{\mu R} \qquad (53)$$

where p_{ss} is the sagittal sinus pressure, $p_{ss} = 2$ mmHg; μ is viscosity and R is resistance to CSF outflow, $\mu R = 80$ mmHg·s/μl (Jones, Deane & Bucknall, 1987; Moazen et al., 2016). Three flow rates are used in the numerical modelling as boundary conditions (Eqs. (54) and (55)) and the storage effect Q_p is modelled by the poroelastic model itself because the storage capacity is an inherent characteristic of porous media.

Details about the experiments can be found in the paper by Vindedal et al. (2016). The geometry used for the validation is a spherical shell, bounded by two concentric spheres. This is a common practice if the focus is on the mechanical characteristics of the system (Tully & Ventikos, 2011). The ICP is almost constant spatially so a relative coarse mesh is used for the model – the total number of 4-node tetrahedral elements is 1105. The radius of the outer sphere ($r = c$) is 4.95 mm and the radius of the inner sphere ($r = a$) is 1.05 mm (Fig. 12). The volume that lies between these two spheres is the domain for numerical modelling, which represents the brain parenchyma of a mouse. The dimensions of the model are derived to make the volume of the parenchyma equivalent to the volume of a mouse (C57BL/6 J) brain (Badea, Ali-Sharief and Johnson, 2007; Vindedal et al., 2016).

The four-compartmental poroelastic model described in Section 3 is used for the modelling. The boundary conditions for the arterial compartment, the arteriole/capillary compartment and the venous compartment are the same as listed in Table 1, where the outer spherical surface represents the cortical surface and the inner surface represents the ventricular wall. For the CSF/ISF compartment, modifications of boundary conditions are made to mimic the setup of an infusion test. More specifically, Robin boundary conditions are applied at both inner and outer spherical surfaces (Sobey et al., 2012). At
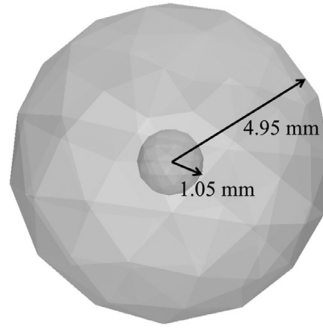
Fig. 12. Spherical shell model used for the modelling of an infusion test.

Table 3
Parameters used in the validation of the 4-MPET model.

Parameters	Values	Units	Parameters	Values	Units
$\alpha_{a,c}$	0.25		S_v	1.5×10^{-5}	m^2N^{-1}
α_e	0.49		$k_{a,c,v}$	1.0×10^{-10}	m^2
α_v	0.01		k_e	1.5×10^{-8}	m^2
λ	505	Pa	ω_{ac}	1.5×10^{-19}	$\text{m}^2\text{N}^{-1}\text{s}^{-1}$
G	216	Pa	ω_{cv}	1.5×10^{-19}	$\text{m}^2\text{N}^{-1}\text{s}^{-1}$
$S_{a,c}$	3.0×10^{-4}	m^2N^{-1}	ω_{ev}	1.0×10^{-13}	$\text{m}^2\text{N}^{-1}\text{s}^{-1}$
S_e	4.0×10^{-4}	m^2N^{-1}	ω_{ce}	1.0×10^{-20}	$\text{m}^2\text{N}^{-1}\text{s}^{-1}$

the outer surface boundary ($r = c$), which represents the cortical surface, the boundary condition describes the conservation of CSF in the subarachnoid space,

$$Q_R = \frac{\pi d^4}{128 \mu L} \left(p|_{r=a} - p \right) - 4\pi c^2 \frac{k}{\mu} \frac{\partial p}{\partial r} + Q_i \tag{54}$$

and it is assumed that at this surface the displacement is zero. At the inner surface boundary ($r = a$), which represents the ventricular wall, the boundary condition also defines the flux conservation of CSF,

$$4\pi a^2 \frac{\partial u}{\partial t} = -\frac{\pi d^4}{128 \mu L} \left(p - p|_{r=c} \right) + 4\pi a^2 \frac{k}{\mu} \frac{\partial p}{\partial r} + Q_p \tag{55}$$

and there are no displacement constraints at this boundary. From the geometry of the model, it can be derived that the length of the aqueduct (a single thin canal connecting the ventricles to the subarachnoid space) is $L = c - a = 3.9$ mm, and the diameter of the aqueduct $d = 0.04$ mm (Feng et al., 2009). The flow in the aqueduct is assumed to be Poiseuille flow (Sobey et al., 2012), based on which the first terms on the right-hand sides of Eqs. (54) and (55) can be decided. The permeability for the CSF/ISF compartment k_e is 1.5×10^{-8} m^2 and the viscosity μ_e is 8.0×10^{-4} N·s/m^2 (Binder, Papadopoulos, Haggie & Verkman, 2004; Oshio, Watanabe, Song, Verkman & Manley, 2005); other parameters used in the validation test are listed in Table 3 (Combe et al., 2016; Wilde et al., 2017). The time-step used in the modelling is $\Delta t = 1$ s.

In the experiments (Vindedal et al., 2016), six wild types of C57BL/6 J mouse were tested. The intracranial pressure (ICP) recordings in response to injections of artificial cerebrospinal fluid are plotted in Fig. 13. The results from numerical modelling are plotted in the same figure by the black line.

It can be seen that the numerical results fall within the range of experimental data. This validation test demonstrates that the change of ICP during an infusion test can be successfully modelled by the numerical simulation. Both the infusion and decay stages, which are separated by the peak of ICP, are distinctively captured. It should be noted that the high-frequency fluctuations of ICP from experiments are mainly caused by arterial pressure pulsations, which are not considered in the numerical modelling due to the lack of experimental data to quantify the input parameters. Therefore, the plot from numerical results is smooth without pulsatile fluctuations.

6. Model application to three-dimensional subject-specific human brain

The numerical solver of the three-dimensional MPET model can be applied to biological systems to investigate fluid flow, transport phenomena and deformation of tissue, etc. A successful simulation generally requires three categories of data to be fed into the MPET solver: finite element mesh, material parameters and boundary conditions. As an example, a schematic illustration of using the n-MPET model for human brain is shown in Fig. 14, where n represents the number of fluid networks. The finite element mesh reflects the geometric characteristics and also controls the spatial resolution of the numerical results; the material parameters are required to completely define the governing equations Eqs. (3)–(7) of the
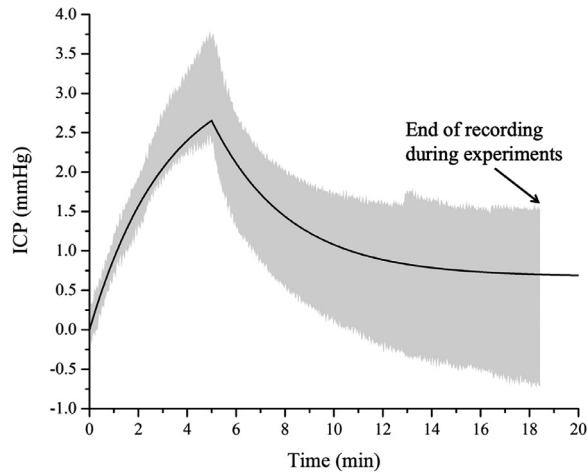
Fig. 13. Comparison between numerical results and experiments for the infusion test. The light grey area represents the range of experimental data and the solid line is the plot of numerical results.
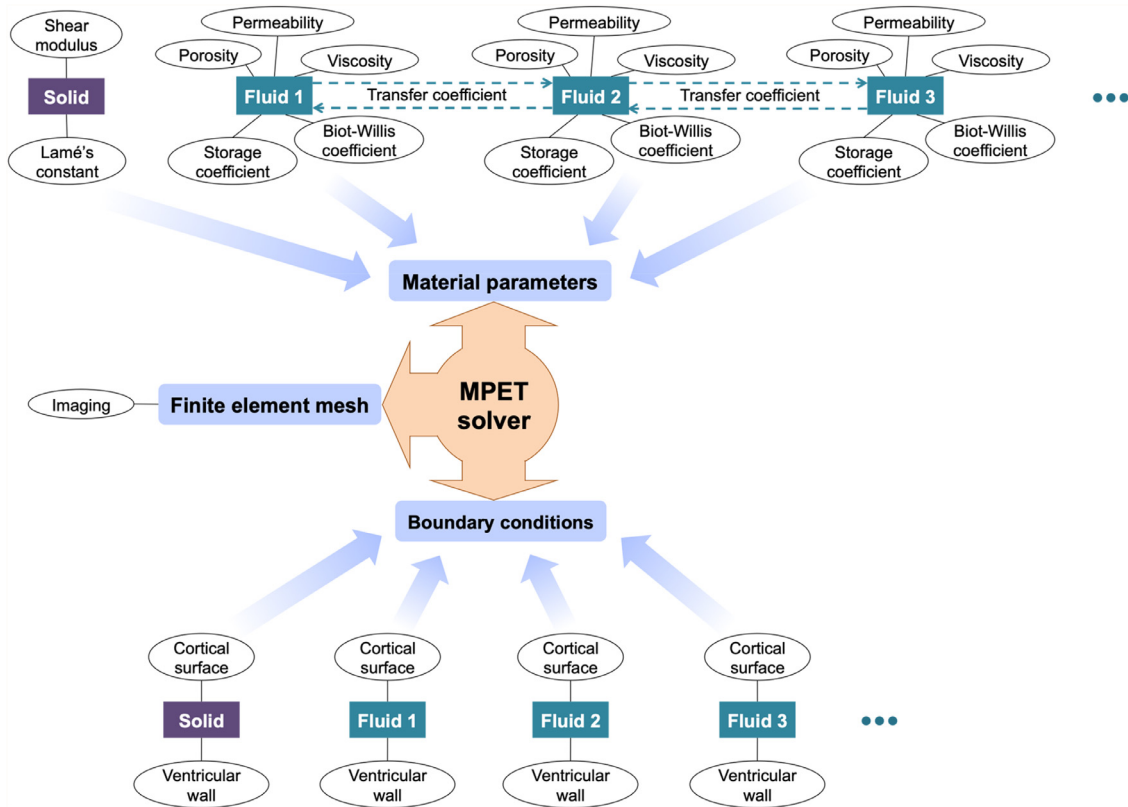
Fig. 14. Subject-specific modelling of human brain using the three-dimensional *n*-MPET model.

solid phase and fluid networks; the boundary conditions make the entire system well posed and introduce supplementary physical meaning to the problem of interest.

For biological systems, the individual variability and inherent complexity make it necessary to conduct numerical modelling in a subject-specific manner so quantitative understanding of their structures and functions in health and disease can be obtained (Taylor et al., 1999; Winslow, Trayanova, Geman & Miller, 2012). To achieve such a goal by using the MPET model, ideally, every element in the ellipse in Fig. 14 should use subject-specific expressions or values. However, the reality is that many of them are not available on a subject-specific basis; this limitation is further discussed in Section 7. In the examples presented in this section, the subject-specific requirements are considered in the modelling from three aspects

Table 4
Parameters used in the subject-specific modelling by the 4-MPET model.

Parameters	Values	Units	Parameters	Values	Units
$\alpha_{a,c}$	0.25		S_e	3.9×10^{-4}	m^2N^{-1}
α_e	0.49		S_v	1.5×10^{-5}	m^2N^{-1}
α_v	0.01		$k_{a,c,e,v}$	1.0×10^{-10}	m^2
λ	505	Pa	ω_{ac}	1.5×10^{-7}	$m^2N^{-1}s^{-1}$
G	216	Pa	ω_{cv}	1.5×10^{-7}	$m^2N^{-1}s^{-1}$
L	70×10^{-3}	m	ω_{ev}	1.0×10^{-6}	$m^2N^{-1}s^{-1}$
d	3×10^{-3}	m	ω_{ce}	1.0×10^{-8}	$m^2N^{-1}s^{-1}$
p_{bp}	650	Pa	R	8.5×10^{13}	m^{-3}
$S_{a,c}$	2.9×10^{-4}	m^2N^{-1}	Q_p	5.8×10^{-9}	m^3s^{-1}

(Guo et al., 2018): First, the finite element meshes are generated from T1-weighted magnetic resonance (T1w-MR) images, which can represent anatomically accurate geometry of the individual brain. Second, the permeability of the cerebrospinal fluid/interstitial fluid (CSF/ISF) compartment is extracted from diffusion-weighted imaging (DWI), which can provide a heterogeneous and anisotropic permeability distribution for the brain parenchyma. Third, the boundary condition for the arterial compartment at the cortical surface is obtained from clinical measurements. The details about these three aspects of the subject-specific brain modelling pipeline can be found in the paper by Guo et al. (2018). All the other material parameters and boundary conditions (Tables 1 and 4) are either from literature or previously tested in numerical modelling (Smillie et al., 2005; Tully & Ventikos, 2011; Vardakis et al., 2013).

The arterial blood supply to the entire brain, including carotid arteries (left and right) and vertebral arteries (left and right), was obtained through a combination of ambulatory blood pressure measurements, clinical ultrasound flow measurements and mathematical modelling (Lassila et al., 2018). A lumped parameter circulation model (LPCM) (Ursino, 1998) was used to translate spot measurements collected at 15-min intervals to continuous waveforms of arterial blood flow, which are used as boundary conditions for the arterial compartment at the cortical surface (Guo et al., 2018). Each waveform has duration of about one second and their amplitudes vary during the day. Here two specific moments are chosen as indicative of the subject's activity in a period of 24 h – the first one is high activity (e.g. exercise) identified by the highest peak value of the arterial blood supply; and the second one is low activity (e.g. rest or sleep) identified by the lowest peak value. To ensure that the numerical results represent steady states, in every simulation the same waveform is repeatedly used 50 times and only the last output is regarded as the final result. This criterion of running 50 cycles is determined by comparing the final results after different numbers of cycles and it is found more than 50 cycles only generate negligible differences. All the simulations in this section use a fixed time-step of 0.1 s.

Three variables are selected from the output files to link mechanistic modelling with clinical practice: Blood perfusion is defined as the filtration velocity (Darcy velocity) of the arteriole/capillary compartment, i.e. $\mathbf{v}_c$; CSF/ISF clearance is defined as the Darcy velocity of the CSF/ISF compartment, i.e. $\mathbf{v}_e$; and the deformation of tissue is measured by the displacements of finite element nodes, i.e. $\mathbf{u}$. In this section, the results from subject-specific modelling are compared between age and gender matched subjects in the context of investigating the effect of smoking on cerebral fluid transport. It should be noted that the comparisons do not indicate any statistical significance but focus on individual differences, which demonstrate the ability of the MPET model to generate clinically relevant output from subject-specific input data. All of the numerical results presented in this section were obtained from the subject-specific brain modelling pipeline of the VPH-DARE@IT project (Guo et al., 2018), which was implemented on the MULTIX platform (Kasztelnik et al., 2017). The study was approved by the joint ethics committee of the Health Authority Venice 12 and the IRCCS San Camillo (Protocol number 2014.08), and all participants gave informed consent prior to participation in the study.

Chronic cigarette smoking is generally recognised as a lifestyle factor that can cause neurobiological deficits and disturbances in brain perfusion (Durazzo, Mattsson & Weiner, 2014), which are related to stroke and vascular dementia, etc (Rogers et al., 1983). To test the ability of the MPET model to capture the differences between smokers and non-smokers, two subjects are simulated using the 4-MPET model; both are healthy, female and 68 years old. The geometry of the smoking subject's brain is discretised by 2 294 536 tetrahedral elements, and 2 533 529 elements are used for the non-smoking subject's brain. Both high and low activities are modelled for each subject so in total there are four scenarios.

First, the total arterial blood supply to the brain in these four scenarios is plotted in Fig. 15. It shows that at both high activity (e.g. exercise) and low activity (e.g. rest or sleep), the total arterial blood flow to the brain is lower in the case of the smoking subject than the non-smoking subject. This is in agreement with the physiological observations that show cigarette smoking impairs cerebral blood flow (Rogers, Meyer, Judd & Mortel, 1985; Yamashita, Kobayashi, Yamaguchi, Kitani & Tsunematsu, 1988; Toda & Okamura, 2016), which is due to cerebral vascular dysfunction and has been identified as a major clinical feature of Alzheimer's disease (de la Torre, 2012).

Next, the differences between high and low activities are compared between smoking and non-smoking subjects. The contours in Figs. 16–18 are obtained by conducting the following calculation at every node in the entire domain,

$$\mathbf{v}_{diff} = \mathbf{v}_{high} - \mathbf{v}_{low} \tag{56}$$

where $\mathbf{v}_{diff}$ is the difference between high activity ($\mathbf{v}_{high}$) and low activity ($\mathbf{v}_{low}$); here $\mathbf{v}$ can be any vector (or scalar) from the output variables. In this part, the filtration velocity (Darcy velocity) of the arteriole/capillary compartment $\mathbf{v}_c$ is used to
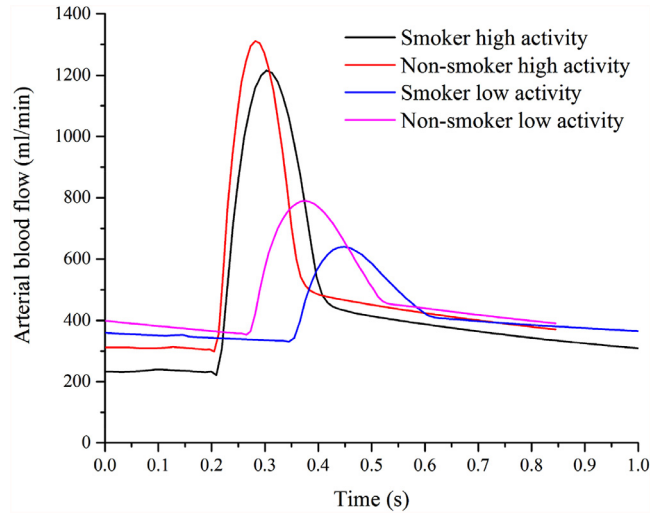
Fig. 15. The total arterial blood supply to the brain at high and low activities between a smoking subject and a non-smoking subject.

a. Smoker – high activity.

b. Non-smoker – high activity.

c. Smoker – low activity.

d. Non-smoker – low activity.

e. Smoker – difference between high and low activities.

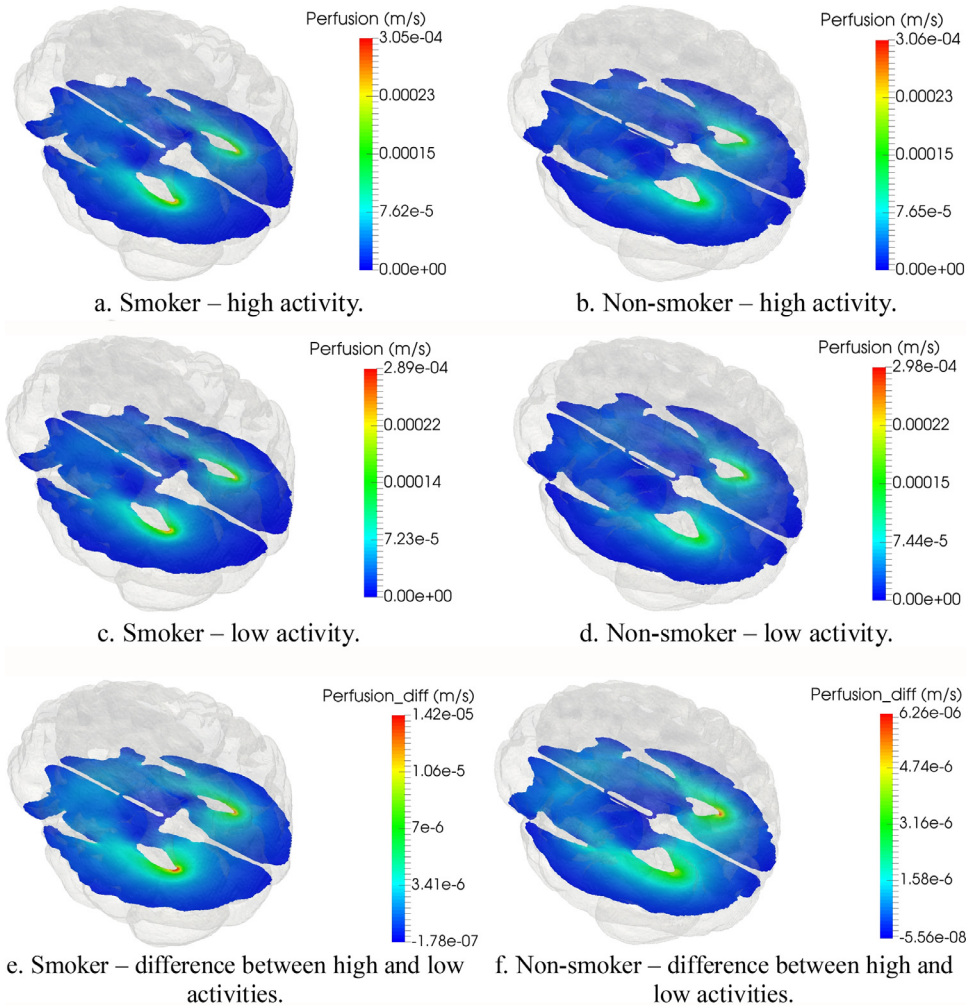f. Non-smoker – difference between high and low activities.

Fig. 16. Perfusion contours of the smoking and non-smoking subjects in high and low activities. (a) and (b) show the perfusion in a horizontal plane in high activity (e.g. exercise); (c) and (d) show the perfusion in the same plane in low activity (e.g. rest); and (e) and (f) show the difference between high and low activities, calculated from Eq. (56).
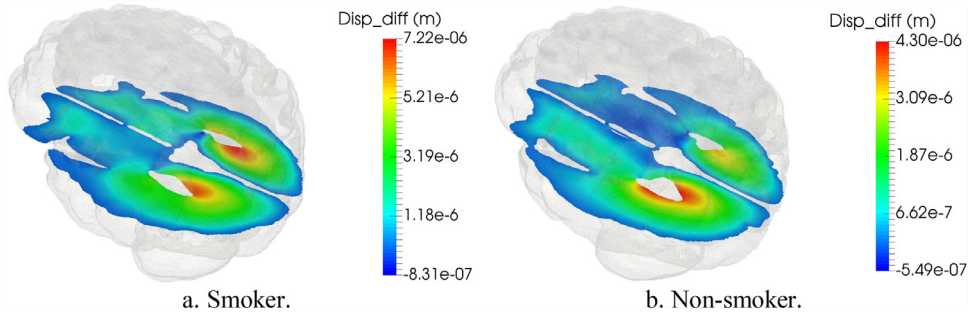
Fig. 17. Deformation differences between high and low activities (horizontal planes, smoker vs. non-smoker).
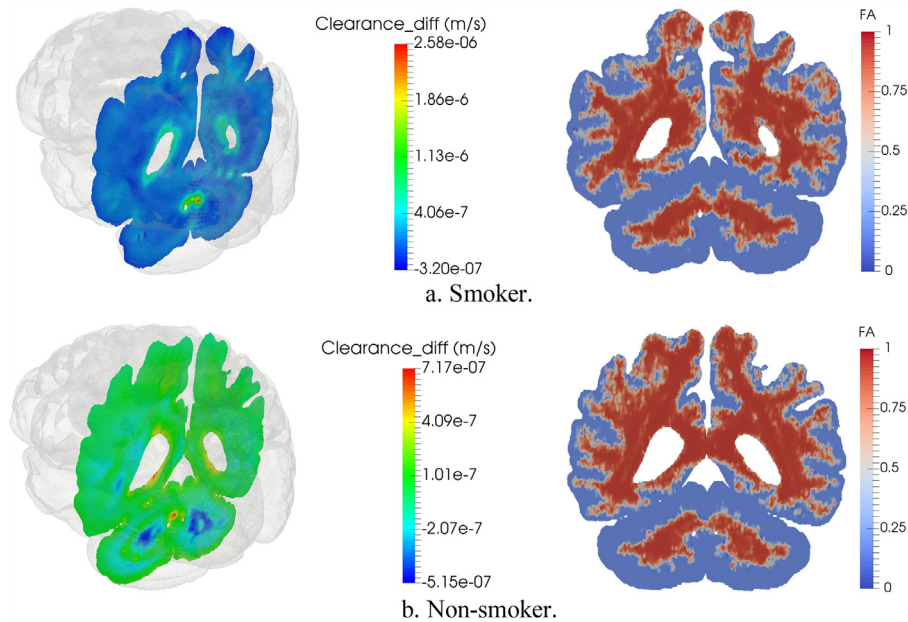

Fig. 18. CSF/ISF clearance differences between high and low activities (coronal planes, smoker vs. non-smoker). The right column shows the fractional anisotropy (FA) derived from diffusion-weighted imaging, where the slices correspond to the cross-sectional planes in the left column.

show brain perfusion; the magnitude of the displacement vector **u** is used to show the tissue deformation; and the Darcy velocity of the CSF/ISF compartment $\mathbf{v}_e$ is used to show CSF/ISF clearance.

One important difference between smokers and non-smokers is brain perfusion – smokers show lower perfusion than non-smokers (hypoperfusion), both globally and in multiple regions (Durazzo, Meyerhoff & Murray, 2015; Siennicki-Lantz, Reinprecht, Wollmer & Elmståhl, 2008), which can be seen from the numerical results. In high and low activities, the perfusion of the smoking subject has a maximum value of 3.05×10^{-4} m/s and 2.89×10^{-4} m/s, respectively (Fig. 16a, c); while the non-smoking subject has a higher maximum value of 3.06×10^{-4} m/s and 2.98×10^{-4} m/s, respectively (Fig. 16b, d). Moreover, it can be seen that the smoking subject shows greater difference between high and low activities, i.e. the brain perfusion of the smoking subject is not as stable as the non-smoking subject in the 24-hour period (Fig. 16e, f). The contours exhibit a similar pattern, e.g. the closer to the posterior horns of lateral ventricles, the greater the difference. However, the magnitude of the difference of the smoking subject is more than twice the value of the non-smoking subject. The differences of brain parenchyma deformation between high and low activities show similar magnitudes and patterns between the smoking and non-smoking subjects (Fig. 17), where the values are at the same order of magnitude and largest differences are around the lateral ventricles.

CSF of the central nervous system (CNS) is critical for the clearance of solute from the brain. The variables related to the CSF/ISF compartment show marked differences between smoking and non-smoking subjects, which is mainly due to the subject-specific permeability maps used for the CSF/ISF compartment. In the modelling, every fluid network is assigned a base permeability value k_i (Table 4). For the arterial compartment (k_a), arteriole/capillary compartment (k_c) and the venous compartment (k_v), the permeability is assumed to be an isotropic and homogeneous property due to the lack of data from clinical measurements; however, for the CSF/ISF compartment (k_e), a three-dimensional permeability map was generated

from processing diffusion-weighted imaging (DWI) for every subject (Guo et al., 2018; Ravikumar, Gooya, Çimen, Frangi & Taylor, 2018), which assigns an anisotropic permeability tensor (dimensionless) for each tetrahedral element in the finite element mesh. In the simulations, the value of permeability for the CSF/ISF compartment is the base permeability multiplied by the dimensionless permeability tensor.

For the differences of CSF/ISF clearance between high and low activities, it can be seen from Fig. 18 that both the patterns and magnitudes are different between the smoking and non-smoking subjects. The non-smoking subject shows a more uniform field, while the smoking subject has a greater gradient. This can also be seen from the magnitude perspective, where it shows the maximum difference of CSF/ISF clearance is about 3.5 times higher in the smoking subject. This indicates that the smoking subject has greater fluctuations of CSF/ISF clearance in the 24-hour period. The dimensionless fractional anisotropy (FA) derived from diffusion-weighted imaging of the two subjects is shown in the right column of Fig. 18. The fractional anisotropy indicates the deviation from pure isotropic diffusion and is used to quantify the microstructural integrity of the white matter (Basser & Pierpaoli, 1996). Previous studies showed that smoking was associated with reduced microstructural integrity of the white matter, such as white matter hyperintensities (WMH) (Gons et al., 2011; Habes et al., 2016). From an imaging point of view, fractional anisotropy is believed to decrease with impaired structural integrity of the white matter (Le Bihan et al., 2001; Pierpaoli, Jezzard, Basser, Barnett & Di Chiro, 1996; Wardlaw, Hernández & Muñoz-Maniega, 2015); it can be seen from Fig. 18 that the value of fractional anisotropy is indeed smaller in the smoking subject, especially in the parietal lobes.

7. Discussion

The computational platform of the three-dimensional multiple-network poroelastic model (n-MPET) can be used to conduct steady-state static and transient quasi-static analyses of porous biological systems, such as brain parenchyma, kidney tissue and bone tissue. The in-house numerical code is written in Fortran 95/2003, and will later be released as open source. It has a flexible structure in the following aspects. First, the number of fluid networks n is not a fixed number but can be customised to specific applications. On the one hand, latest development in the understanding of physiology, such as the glymphatic system, which postulates that waste products are cleared from the brain via a glia-dependent mechanism, analogous to the lymphatic system in other organs (Iliff et al., 2012; Nedergaard, 2013), can be added to the numerical model by increasing the value of n. On the other hand, the number n can also be reduced for validation purposes or applications where additional fluid networks have negligible influences on the problem of interest. Second, the material properties and boundary conditions can use pre-defined default values in the code or subject-specific data if available. The difference in execution is to import extra data files into the solver. Third, the pre-processing and post-processing support various formats and open-source software, such as Netgen (Schöberl, 1997), ISO2Mesh (Fang & Boas, 2009), ParaView (Ayachit, 2015) and Mayavi (Ramachandran & Varoquaux, 2011), which gives users the freedom to choose the one that they are most familiar with.

Several limitations still exist in the current model. First, the values of material properties are not the most accurate from a physiological perspective. For example, there was research showing the properties (e.g. Young's modulus) of the white and grey matter are different (Budday et al., 2015; Christ et al., 2010); however, many numerical models (Levine, 2000; Tully & Ventikos, 2009; Wirth & Sobey, 2006), including the one presented in this paper, still treat the brain parenchyma as homogeneous material due to the lack of quantitative experimental data of human brain. In this aspect, magnetic resonance elastography (MRE), which is a non-invasive imaging technique to quantify mechanical properties of tissue (Feng et al., 2018; Green, Bilston & Sinkus, 2008), can offer more realistic values for numerical modelling. Recent research also suggested that the typical permeability currently used in modelling was too high by one or two orders of magnitude (Holter et al., 2017), which needs further investigation as well. Moreover, the parameters used in numerical modelling need to be validated. This has two-fold meaning: First, the values themselves must by physiologically reasonable; and second, the numerical results obtained from these values must also be validated against experimental or clinical data.

Second, more effort needs to be put into refining the underlying biological and mechanical mechanisms of the multiple-network poroelastic model used for biological systems. One example of such physiological mechanisms is the transfer of fluids between different fluid compartments. In the current model, this transfer purely depends on hydrostatic pressure gradients, while in the biological context it is more likely to be driven by more complicated biological processes, such as via osmotic pressure – a fact for biological fluids that have a lot of minerals including ions dissolved in them. This limitation can be overcome by implementing empirical relationships once they are validated (Tully & Ventikos, 2011). Another example in the aspect of mechanical mechanisms is the cross-porosity storage effect (Mehrabian & Abousleiman, 2017; Vardakis et al., 2017). In the future, it is worth exploring the differences in numerical results between models neglecting and employing such effects.

Third, as already pointed out in Section 6, the subject-specific modelling at the current stage has not reached an ideal level of personalisation in order to differentiate between subjects. The higher the complexity of the model, more factors need to be specified. The main reason for this limitation is that the data are not available from experiments or *in vivo* measurements. It can be seen from Fig. 14 that for a complete subject-specific simulation, every element in the ellipse should be personalised, which itself is a non-trivial task. A solution that can improve this situation is to translate more physiological understanding into mechanical relationships and mathematical expressions, and implement them into the numerical model; then subject-specific data can be fed into the modelling. Similar to other interdisciplinary research, the difficulty here is

to find connections across the boundaries of disciplines. Ideally, the entire workflow to develop the model should form a virtuous circle – better understanding of physiology helps improve numerical models and more advanced numerical models provide testing beds for testing hypotheses and developing theories.

8. Conclusions

A finite element model for biological systems has been developed based on the multiple-network poroelastic theory (n-MPET). The governing equations were defined for the mathematical model, and boundary conditions applicable to the cerebral environment were given to provide supplementary physical meaning from a physiological point of view. The model was implemented into an in-house finite element code. The numerical model was verified against the analytical solutions of the Terzaghi's problem and the Mandel's problem, and validated against experimental data from infusion tests on mouse brain. The model was successfully applied to three-dimensional subject-specific modelling of water transport in the cerebral environment, which included anatomically realistic geometry, personalised permeability map for the diffusion of cerebrospinal fluid, and subject-specific arterial blood supply to the brain. The numerical results were compared between smoking and non-smoking subjects, which showed hypoperfusion in the brain of the smoking subject.

The three-dimensional n-MPET model has been demonstrated to be capable of capturing the spatio-temporal fluid transport in biological systems across different scales. Clinically relevant mechanisms, such as blood perfusion, cerebrospinal fluid clearance and tissue deformation, can be visualised in fully three-dimensional anatomically realistic models. The numerical code will later be released as open source, which will create an open and flexible platform for researchers to tailor the numerical tool for their specific biomechanical applications, which can help translate computational modelling paradigms into clinical practice.

Declaration of Competing Interest

None.

Acknowledgements

References

Abbott, N. J. (2004). Evidence for bulk flow of brain interstitial fluid: Significance for physiology and pathology. *Neurochemistry International, 45*, 545–552.
Abbott, N. J., Rönnbäck, L., & Hansson, E. (2006). Astrocyte-endothelial interactions at the blood-brain barrier. *Nature Reviews Neuroscience, 7*, 41–53.
Abousleiman, Y., Cheng, A. H.-D., Cui, L., Detournay, E., & Roegiers, J.-C. (1996). Mandel's problem revisited. *Géotechnique, 46*(2), 187–195.
Aifantis, E. C. (1977). Introducing a multi-porous medium. *Developments in Mechanics, 8*, 209–211.
Aifantis, E. C. (1979). Continuum basis for diffusion in regions with multiple diffusivity. *Journal of Applied Physics, 50*(3), 1334–1338.
Aifantis, E. C., & Hill, J. M. (1980). On the theory of diffusion in media with double diffusivity I. basic mathematical results. *The Quarterly Journal of Mechanics and Applied Mathematics, 33*(1), 1–21.
Andersson, N., Malm, J., & Eklund, A. (2008). Dependency of cerebrospinal fluid outflow resistance on intracranial pressure. *Journal of Neurosurgery, 109*, 918–922.
Atkin, R. J., & Craine, R. E. (1976a). Continuum theories of mixtures: Basic theory and historical development. *The Quarterly Journal of Mechanics & Applied Mathematics, 29*(2), 209–244.
Atkin, R. J., & Craine, R. E. (1976b). Continuum theories of mixtures: Applications. *Journal of the Institute of Mathematics and its Applications, 17*, 153–207.
Avezaat, C. J. J., & Eijndhoven, J. H. M. (1984). *Cerebrospinal fluid pulse pressure and craniospinal dynamics. A theoretical, clinical and experimental study* (combined thesis). The Hague: A Jongbloed en Zoon.
Ayachit, U. (2015). *The paraview guide: A parallel visualization application*. Kitware.
Badea, A., Ali-Sharief, A. A., & Johnson, G. A. (2007). Morphometric analysis of the C57BL/6 J mouse brain. *NeuroImage, 37*(3), 683–693.
Bai, M. (1999). On equivalence of dual-porosity poroelastic parameters. *Journal of Geophysical Research, 104*, 10461–10466.
Bai, M., Elsworth, D., & Roegiers, J.-C. (1993). Multiporosity/Multipermeability approach to the simulation of naturally fractured reservoirs. *Water Resources Research, 29*(6), 1621–1633.
Bai, M., Meng, F., Elsworth, D., Abousleiman, Y., & Roegiers, J.-C. (1999). Numerical modelling of coupled flow and deformation in fractured rock specimens. *International Journal for Numerical and Analytical Methods in Geomechanics, 23*, 141–160.
Balay, S., Abhyankar, S., Adams, M.F., Brown, J., Brune, P., Buschelman, K. … Zhang, H. (2018a). PETSc Web page http://www.mcs.anl.gov/petsc.
Balay, S., Abhyankar, S., Adams, M. F., Brown, J., Brune, P., Buschelman, K., … Zhang, H. (2018b). *PETSc users manual, ANL-95/11 - Revision 3.9*. Argonne National Laboratory.
Basser, P. J., & Pierpaoli, C. (1996). Microstructural and physiological features of tissues elucidated by quantitative-diffusion-tensor MRI. *Journal of Magnetic Resonance Series B, 111*, 209–219.
Bedford, A., & Drumheller, D. S. (1983). Theories of immiscible and structured mixtures. *International Journal of Engineering Science, 21*(8), 863–960.
Berryman, J. G. (1992). Effective stress for transport properties on inhomogeneous porous rock. *Journal of Geophysical Research, 97*, 17409–17424.

Berryman, J. G. (2002). Extension of poroelastic analysis to double-porosity materials: New technique in microgeomechanics. *Journal of Engineering Mechanics, 128*(8), 840–847.

Berryman, J. G., & Wang, H. F. (1995). The elastic coefficients of double-porosity models for fluid transport in jointed rock. *Journal of Geophysical Research, 100*, 24611–24627.

Binder, D. K., Papadopoulos, M. C., Haggie, P. M., & Verkman, A. S. (2004). In vivo measurement of brain extracellular space diffusion by cortical surface photobleaching. *The Journal of Neuroscience, 24*(37), 8049–8056.

Biot, M. A. (1941). General theory of three-dimensional consolidation. *Journal of Applied Physics, 12*, 155–164.

Biot, M. A. (1955). Theory of elasticity and consolidation for a porous anisotropic solid. *Journal of Applied Physics, 26*, 182–185.

Biot, M. A. (1956). Theory of deformation of a porous viscoelastic anisotropic solid. *Journal of Applied Physics, 27*, 459–467.

Boon, A. J. W., Tans, J. Th. J., Delwel, E. J., Egeler-Peerdeman, S. M., Hanlo, P. W., Wurzer, H. A. L., & Hermans, J. (2000). The Dutch normal-pressure hydrocephalus study how to select patients for shunting? An analysis of four diagnostic criteria. *Surgical Neurology, 53*, 201–207.

Bowen, R. M. (1976). Theory of mixtures. In A. C. Eringen (Ed.). In *Continuum physics: III* (pp. 1–127). New York: Academic Press.

Bowen, R. M. (1982). Compressible porous media models by use of the theory of mixtures. *International Journal of Engineering Science, 20*(6), 697–735.

Budday, S., Nay, R., de Rooij, R., Steinmann, P., Wyrobek, T., Ovaert, T. C., … Guck, J. (2015). Mechanical properties of gray and white matter brain tissue by indentation. *Journal of the Mechanical Behavior of Biomedical Materials, 46*, 318–330.

Chen, D., Wei, J., Deng, Y., Xu, H., Li, Z., Meng, H., … Tang, X. (2018). Virtual stenting with simplex mesh and mechanical contact analysis for real-time planning of thoracic endovascular aortic repair. *Theranostics, 8*(20), 5758–5771.

Choo, J., & Borja, R. I. (2015). Stabilized mixed finite elements for deformable porous media with double porosity. *Computer Methods in Applied Mechanics and Engineering, 293*, 0–23.

Chou, D., Vardakis, J. C., Guo, L., Tully, B. J., & Ventikos, Y. (2016). A fully dynamic multi-compartment poroelastic system: Application to aqueductal stenosis. *Journal of Biomechanics, 49*, 2306–2312.

Christ, A. F., Franze, K., Gautier, H., Moshayedi, P., Fawcett, J., Franklin, R. J. M., … Guck, J. (2010). Mechanical difference between white and gray matter in the rat cerebellum measured by scanning force microscopy. *Journal of Biomechanics, 43*, 2986–2992.

Christensen, K. L., & Mulvany, M. J. (2001). Location of resistance arteries. *Journal of Vascular Research, 38*, 1–12.

Cieslicki, K. (2007). Mathematical modelling of the infusion test. *Polish Journal of Medical Physics and Engineering, 13*(1), 33–54.

Combe, R., Mudgett, J., El Fertak, L., Champy, M.-F., Ayme-Dietrich, E., Petit-Demoulière, B., … Monassier, L. (2016). How does circadian rhythm impact salt sensitivity of blood pressure in mice? A study in two close C57Bl/6 substrains. *PloS one, 11*(4), E0153472.

Coussy, O., Dormieux, L., & Detournay, E. (1998). From mixture theory to Biot's approach for porous media. *International Journal of Solids and Structures, 35*, 4619–4635.

Cryer, C. W. (1963). A comparison of the three-dimensional consolidation theories of Biot and Terzaghi. *The Quarterly Journal of Mechanics and Applied Mathematics, 16*, 401–412.

de Boer, R. (1992). Development of porous media theories – a brief historical review. *Transport in Porous Media, 9*, 155–164.

de Boer, R., & Ehlers, W. (1988). A historical review of the formulation of orous media theories. *Acta Mechanica, 74*, 1–8.

de la Torre, J. C. (2012). Cardiovascular risk factors promote brain hypoperfusion leading to cognitive decline and dementia. *Cardiovascular Psychiatry and Neurology, 2012*, 367516.

Dean, R. H., Gai, X., Stone, C. M., & Minkoff, S. E. (2006). A comparison of techniques for coupling porous flow and geomechanics. *SPE Journal, 11*(1), 132–140.

Detournay, E., & Cheng, A. H.-D. (1993). Fundamentals of poroelasticity. In C. Fairhurst (Ed.), *Comprehensive Rock Engineering: Principles, Practice and Projects, Vol. II, Analysis and Design Methods* (pp. 113–171). Pergamon Press.

Durazzo, T. C., Mattsson, N., & Weiner, M. W. (2014). Smoking and increased Alzheimer's disease risk: A review of potential mechanisms. *Alzheimer's & Dementia, 10*, S122–S145.

Durazzo, T. C., Meyerhoff, D. J., & Murray, D. E. (2015). Comparison of regional brain perfusion levels in chronically smoking and non-smoking adults. *International Journal of Environmental Research and Public Health, 12*, 8198–8213.

Edsbagge, M., Tisell, M., Jacobsson, L., & Wikkelso, C. (2004). Spinal CSF absorption in healthy individuals. *American Journal of Physiology Regulatory, Integrative and Comparative Physiology, 287*, 1450–1455.

Fang, Q., & Boas, D. A. (2009). Tetrahedral mesh generation from volumetric binary and grayscale images. In *Proceedings of the IEEE international symposium on biomedical imaging: from nano to macro, Boston, USA* (pp. 1142–1145).

Feng, X., Papadopoulos, M. C., Liu, J., Li, L., Zhang, D., Zhang, H., … Ma, T. (2009). Sporadic obstructive hydrocephalus in Aqp4 null mice. *Journal of Neuroscience Research, 87*, 1150–1155.

Feng, Y., Zhu, M., Qiu, S., Shen, P., Ma, S., Zhao, X., … Guo, L. (2018). A multi-purpose electromagnetic actuator for magnetic resonance elastography. *Magnetic Resonance Imaging, 51*, 29–34.

Ferronato, M., Castelletto, N., & Gambolati, G. (2010). A fully coupled 3-D mixed finite element model of Biot consolidation. *Journal of Computational Physics, 229*, 4813–4830.

Gibson, R. E., Gobert, A., & Schiffman, R. L. (1990). On Cryer's problem with large displacements and variable permeability. *Géotechnique, 40*, 627–631.

Gons, R. A. R., van Norden, A. G. W., de Laat, K. F., van Oudheusden, L. J. B., van Uden, I. W. M., Zwiers, M. P., … de Leeuw, F.-E. (2011). Cigarette smoking is associated with reduced microstructural integrity of cerebral white matter. *Brain : a journal of neurology, 134*, 2116–2124.

Green, M. A., Bilston, L. E., & Sinkus, R. (2008). In vivo brain viscoelastic properties measured by magnetic resonance elastography. *NMR in Biomedicine, 21*, 755–764.

Guo, L., Vardakis, J. C., Lassila, T., Mitolo, M., Ravikumar, N., Chou, D., … Ventikos, Y. (2018). Subject-specific multi-poroelastic model for exploring the risk factors associated with the early stages of Alzheimer's disease. *Interface focus, 8*, 20170019.

Gupta, S., Soellinger, M., Boesiger, P., Poulikakos, D., & Kurtcuoglu, V. (2009). Three-dimensional computational modeling of subject-specific cerebrospinal fluid flow in the subarachnoid space. *Journal of Biomechanical Engineering, 131*(2), 021010.

Gupta, S., Soellinger, M., Grzybowski, D. M., Boesiger, P., Biddiscombe, J., Poulikakos, D., & Kurtcuoglu, V. (2010). Cerebrospinal fluid dynamics in the human cranial subarachnoid space: An overlooked mediator of cerebral disease. I. Computational model. *Journal of the Royal Society Interface, 7*, 1195–1204.

Habes, M., Erus, G., Toledo, J. B., Zhang, T., Bryan, N., Launer, L. J., … Davatzikos, C. (2016). White matter hyperintensities and imaging patterns of brain aging in the general population. *Brain : A Journal of Neurology, 139*, 1164–1179.

Hoffman, J. I., & Spaan, J. A. (1990). Pressure-flow relations in coronary circulation. *Physiological Reviews, 70*(2), 331–390.

Holter, K. E., Kehlet, B., Devor, A., Sejnowski, T. J., Dale, A. M., Omholt, S. W., … Pettersen, K. H. (2017). Interstitial solute transport in 3D reconstructed neuropil occurs by diffusion rather than bulk flow. *Proceedings of the National Academy of Sciences of the United States of America, 114*(37), 9894–9899.

Iliff, J. J., Wang, M., Liao, Y., Plogg, B. A., Peng, W., Gundersen, G. A., … Nedergaard, M. (2012). A paravascular pathway facilitates CSF flow through the brain parenchyma and the clearance of interstitial solutes, including Amyloid β. *Science Translational Medicine, 4*, 147ra111.

Jones, H. C., Deane, R., & Bucknall, R. M. (1987). Developmental changes in cerebrospinal fluid pressure and resistance to absorption in rats. *Developmental Brain Research, 33*, 23–30.

Juniewicz, H., Kasprowicz, M., Czosnyka, M., Czosynka, Z., Gizewski, S., Dzik, M., & Pickard, J. D. (2005). Analysis of intracranial pressure during and after the infusion test in patients with communicating hydrocephalus. *Physiological Measurement, 26*, 1039–1048.

Kaczmarek, M., & Subramaniam, R. P. (1997). The hydromechanics of hydrocephalus: Steady-state solutions for cylindrical geometry. *Bulletin of Mathematical Biology, 59*(2), 295–323.

Kannan, K., & Rajagopal, K. R. (2008). Flow through porous media due to high pressure gradients. *Applied Mathematics and Computation, 199*, 748–759.

Kasztelnik, M., Coto, E., Bubak, M., Malawski, M., Nowakowski, P., Arenas, J., … Frangi, A. F. (2017). Support for Taverna workflows in the VPH-Share cloud platform. *Computer Methods and Programs in Biomedicine, 146*, 37–46.

Khalili, N. (2003). Coupling effects in double porosity media with deformable matrix. *Geophysical Research Letters, 30*(22), 2153.

Kim, J., Sonnenthal, E. L., & Rutqvist, J. (2012). Formulation and sequential numerical algorithms of coupled fluid/heat flow and geomechanics for multiple porosity materials. *International Journal for Numerical Methods in Engineering, 92*, 425–456.

Koh, L., Zakharov, A., & Johnston, M. (2005). Integration of the subarachnoid space and lymphatics: Is it time to embrace a new concept of cerebrospinal fluid absorption. *Fluids and Barriers of the CNS, 2*, 6.

Lassila, T., Di Marco, L. Y., Mitolo, M., Iaia, V., Levedianos, G., Venneri, A., & Frangi, A. F. (2018). Screening for cognitive impairment by model-assisted cerebral blood flow estimation. *IEEE Transactions on Biomedical Engineering, 65*(7), 1654–1661.

Le Bihan, D., Mangin, J.-F., Poupon, C., Clark, C. A., Pappata, S., Molko, N., & Chabriat, H. (2001). Diffusion tensor imaging: Concepts and applications. *Journal of Magnetic Resonance Imaging, 13*, 534–546.

Lee, J., & Smith, N. P. (2012). The multi-scale modelling of coronary blood flow. *Annals of Biomedical Engineering, 40*(11), 2399–2413.

Lei, Y., Han, H., Yuan, F., Javeed, A., & Zhao, Y. (2017). The brain interstitial system: Anatomy, modeling, in vivo measurement, and applications. *Progress in Neurobiology, 157*, 230–246.

Levine, D. N. (2000). Ventricular size in pseudotumor cerebri and the theory of impaired CSF absorption. *Journal of the Neurological Sciences, 177*, 85–94.

Levine, D. N. (2008). Intracranial pressure and ventricular expansion in hydrocephalus: Have we been asking the wrong question? *Journal of the Neurological Sciences, 269*, 1–11.

Logg, A., Mardal, K. A., & Wells, G. (2012). *Automated solution of differential equations by the finite element method: The Fenics book, lecture notes in computational science and engineering*: 84. Berlin: Springer.

Lun, M. P., Monuki, E. S., & Lehtinen, M. K. (2015). Development and functions of the choroid plexus – cerebrospinal fluid system. *Nature Reviews Neuroscience, 16*, 445–457.

Maas, S. A., Ellis, B. J., Ateshian, G. A., & Weiss, J. A. (2012). FEBio: Finite elements for biomechanics. *Journal of Biomedical Engineering, 134*, 011005 -1.

Mandel, J. (1953). Consolidation des sols (étude mathématique). *Géotechnique, 30*, 287–299.

Marmarou, A., Shulman, K., & Rosende, R. M. (1978). A nonlinear analysis of the cerebrospinal fluid system and intracranial pressure dynamics. *Journal of Neurosurgery, 48*, 332–344.

Martinez-Lemus, L. A. (2011). The dynamic structure of arterioles. *Basic & Clinical Pharmacology & Toxicology, 110*, 5–11.

Mehrabian, A., & Abousleiman, Y. N. (2014). Generalized Biot's theory and Mandel's problem of multiple-porosity and multiple-permeability poroelasticity. *Journal of Geophysical Research: Solid Earth, 119*, 2745–2763.

Mehrabian, A., & Abousleiman, Y. N. (2017). Letter to the editor regarding "A fully dynamic multi-compartmental poroelastic system: Application to aqueductal stenosis". *Journal of Biomechanics, 58*, 241–242.

Moazen, M., Alazmani, A., Rafferty, K., Liu, Z.-J., Gustafson, J., Cunningham, M. L., ... Herring, S. W. (2016). Intracranial pressure changes during mouse development. *Journal of Biomechanics, 49*, 123–126.

Mulvany, M. J., & Aalkjaer, C. (1990). Structure and function of small arteries. *Physiological Reviews, 70*(4), 921–961.

Munaf, D., Lee, D., Wineman, A. S., & Rajagopal, K. R. (1993). A boundary value problem in ground water motion analysis – comparisons based on Darcy's law and the continuum theory of mixtures. *Mathematical Modeling and Methods in Applied Science, 3*, 231–248.

Murad, M. A., & Loula, A. F. D. (1994). On stability and convergence of finite element approximations of Biot's consolidation problems. *International Journal for Numerical Methods in Engineering, 37*, 645–667.

Nedergaard, M. (2013). Garbage truck of the brain. *Science (New York, N.Y.), 340*(6140), 1529–1530.

Oshio, K., Watanabe, H., Song, Y., Verkman, A. S., & Manley, G. T. (2005). Reduced cerebrospinal fluid production and intracranial pressure in mice lacking choroid plexus water channel Aquaporin-1. *The FASEB Journal, 19*(1), 76–78.

Paulsen, K. D., Miga, M. I., Kennedy, F. E., Hoopes, P. J., Hartov, A., & Roberts, D. W. (1999). A computational model for tracking subsurface tissue deformation during stereotactic neurosurgery. *IEEE Transactions on Biomedical Engineering, 46*(2), 213–225.

Phillips, P. J., & Wheeler, M. F. (2009). Overcoming the problem of locking in linear elasticity and poroelasticity: A heuristic approach. *Computers & Geosciences, 13*, 5–12.

Pierpaoli, C., Jezzard, P., Basser, P. J., Barnett, A., & Di Chiro, G. (1996). Diffusion tensor MR imaging of the human brain. *Radiology, 201*(3), 637–648.

Praetorius, J. (2007). Water and solute secretion by the choroid plexus. *Pflügers Archiv - European Journal of Physiology, 454*, 1–18.

Preston, G. M., Carroll, T. P., Guggino, W. B., & Agre, P. (1992). Appearance of water channels in Xenopus oocytes expressing red cell CHIP28 protein. *Science (New York, N.Y.), 256*, 385–387.

Prevost, J. H. (1980). Mechanics of continuous porous media. *International Journal of Engineering Science, 18*, 787–800.

Rajagopal, K. R. (2007). On a hierarchy of approximate models for flows of incompressible fluids through porous solids. *Mathematical Models and Methods in Applied Sciences, 17*(2), 215–252.

Rajagopal, K. R., Saccomandi, G., & Vergori, L. (2010). A systematic approximation for the equations governing convection-diffusion in a porous medium. *Nonlinear Analysis: Real World Applications, 11*, 2366–2375.

Rajagopal, K. R., & Tao, L. (1992). Wave propagation in elastic solids infused with fluids. *International Journal of Engineering Science, 30*(9), 1209–1232.

Rajagopal, K. R., & Tao, L. (1995). *Mechanics of mixtures*. New Jersey: World Scientific.

Rajagopal, K. R., & Tao, L. (2005). On the propagation of waves through porous solids. *International Journal of Non-Linear Mechanics, 40*, 373–380.

Rajagopal, K. R., Wineman, A. S., & Gandhi, M. (1986). On boundary conditions for a certain class of problems in mixture theory. *International Journal of Engineering Science, 24*(8), 1453–1463.

Rajagopal, K. R., Yalamanchili, R. C., & Wineman, A. S. (1994). Modeling electro-rheological materials through mixture theory. *International Journal of Engineering Science, 32*(3), 481–500.

Ramachandran, P., & Varoquaux, G. (2011). Mayavi: 3D visualization of scientific data. *IEEE Computing in Science & Engineering, 13*(2), 40–51.

Ravikumar, N., Gooya, A., Çimen, S., Frangi, A. F., & Taylor, Z. A. (2018). Group-wise similarity registration of point sets using Student's t-mixture model for statistical shape models. *Medical Image Analysis, 44*, 156–176.

Reed, M. B. (1984). An investigation of numerical errors in the analysis of consolidation by finite elements. *International Journal for numerical and analytical methods in geomechanics, 8*, 243–257.

Rogers, R. L., Meyer, J. S., Judd, B. W., & Mortel, K. F. (1985). Abstention from cigarette smoking improves cerebral perfusion among elderly chronic smokers. *JAMA, 253*(20), 2970–2974.

Rogers, R. L., Meyer, J. S., Shaw, T. G., Mortel, K. F., Hardenberg, J. P., & Zaid, R. R. (1983). Cigarette smoking decreases cerebral blood flow suggesting increased risk for stroke. *JAMA, 250*(20), 2796–2800.

Rohan, E., & Cimrman, R. (2012). Multiscale Fe simulation of diffusion-deformation processes in homogenized dual-porous media. *Mathematics and Computers in Simulation, 82*, 1744–1772.

Rohan, E., & Lukeš, V. (2017). Modeling large-deforming fluid-saturated porous media using an Eulerian incremental formulation. *Advances in Engineering Software, 113*, 84–95.

Samohyl, I. (1987). *Thermodynamics of irreversible processes in fluid mixtures*. Leipzig: Teubner.

Sandhu, R. S., & Wilson, E. L. (1969). Finite-element analysis of seepage in elastic media. *Journal of the Engineering Mechanics Division, 95*(3), 641–652.

Schanz, M., & Diebels, S. (2003). A comparative study of Biot's theory and the linear theory of porous media for wave propagation problems. *Acta Mechanica, 161*, 213–235.

Schiffman, R. L., Chen, A. T.-F., & Jordan, J. C. (1969). An analysis of consolidation theories. *Journal of the Soil Mechanics and Foundations Division, 95*(1), 285–312.

Schöberl, J. (1997). NETGEN – An advancing front 2D/3D-mesh generator based on abstract rules. *Computing and Visualization in Science, 1*(1), 41–52.

Siennicki-Lantz, A., Reinprecht, F., Wollmer, P., & Elmståhl, S. (2008). Smoking-related changes in cerebral perfusion in a population of elderly man. *Neuroepidemiology, 30*, 84–92.

Simon, M. J., & Iliff, J. J. (2016). Regulation of cerebrospinal fluid (CSF) flow in neurodegenerative, neurovascular and neuroinflammatory disease. *Biochimica et Biophysica Acta, 1862*, 442–451.

Sivaloganathan, S., Stastna, M., Tenti, G., & Drake, J. M. (2005). A viscoelastic approach to the modelling of hydrocephalus. *Applied Mathematics and Computation, 163*, 1097–1107.

Skempton, A. W. (1954). The pore-pressure coefficients A and B. *Géotechnique, 4*(4), 143–147.

Smillie, A., Sobey, I., & Molnar, Z. (2005). A hydroelastic model of hydrocephalus. *Journal of Fluid Mechanics, 539*, 417–443.

Smith, N. P., Pullan, A. J., & Hunter, P. J. (2002). An anatomically based model of transient coronary blood flow in the heart. *SIAM Journal on Applied Mathematics, 62*(3), 990–1018.

Sobey, I., Eisentrager, A., Wirth, B., & Czosnyka, M. (2012). Simulation of cerebral infusion tests using a poroelastic model. *International Journal of Numerical Analysis and Modelling, 3*(1), 52–64.

Subramanian, S. C., & Rajagopal, K. R. (2007). A note on the flow through porous solids at high pressures. *Computers and Mathematics with Applications, 53*, 260–275.

Tao, L., & Rajagopal, K. R. (1993). Unsteady diffusion of fluids through a non-linearly elastic cylindrical annulus. *International Journal of Non-Linear Mechanics, 28*(1), 43–55.

Taylor, C. A., Draney, M. T., Ku, J. P., Parker, D., Steele, B. N., Wang, K., & Zarins, K. (1999). Predictive medicine: Computational techniques in therapeutic decision-making. *Computer Aided Surgery, 4*, 231–247.

Terzaghi, K. (1925). *Erdbaumechanik auf bodenphysikalischer grundlage*. Vienna: F. Duticke.

Thigpen, L., & Berryman, J. G. (1985). Mechanics of porous elastic materials containing multiphase fluid. *International Journal of Engineering Science, 23*(11), 1203–1214.

Toda, N., & Okamura, T. (2016). Cigarette smoking impairs nitric oxide-mediated cerebral blood flow increase: Implications for Alzheimer's disease. *Journal of Pharmacological Sciences, 131*, 223–232.

Tortora, G. J., & Derrickson, B. (2009). *Principles of anatomy and physiology* (12th). John Wiley & Sons, Inc.

Truesdell, C. (1957a). Sulle basi della termomeccanica, Nota I. *Rendiconti Lincei, 22*, 33–38.

Truesdell, C. (1957b). Sulle basi della termomeccanica, Nota II. *Rendiconti Lincei, 22*, 158–166.

Truesdell, C. (1962). Mechanical basis of diffusion. *Journal of Chemical Physics, 37*(10), 2336–2344.

Truesdell, C. (1984). *Rational thermodynamics* (2nd). New York: Springer Verlag.

Tully, B., & Ventikos, Y. (2009). Coupling poroelasticity and CFD for cerebrospinal fluid hydrodynamics. *IEEE Transactions on Biomedical Engineering, 56*(6), 1644–1651.

Tully, B., & Ventikos, Y. (2011). Cerebral water transport using multiple-network poroelastic theory: Application to normal pressure hydrocephalus. *Journal of Fluid Mechanics, 667*, 188–215.

Ursino, M. (1998). Interaction between carotid baroregulation and the pulsating heart: A mathematical model. *American Journal of Physiology, 275*(5), H1733–H1747.

Vankan, W. J., Huyghe, J. M., Janssen, J. D., & Huson, A. (1996). Poroelasticity of saturated solids with an application to blood perfusion. *International Journal of Engineering Science, 34*(9), 1019–1031.

Vardakis, J. C., Chou, D., Guo, L., Tully, B. J., & Ventikos, Y. (2017). Response to letter to the editor concerning "A fully dynamic multi-compartmental poroelastic system: Application to aqueductal stenosis". *Journal of Biomechanics, 58*, 243–246.

Vardakis, J. C., Chou, D., Tully, B. J., Hung, C. C., Lee, T. H., Tsui, P.-H., & Ventikos, Y. (2016). Investigating cerebral oedema using poroelasticity. *Medical Engineering & Physics, 38*, 48–57.

Vardakis, J. C., Tully, B. J., & Ventikos, Y. (2013). Exploring the efficacy of endoscopic ventriculostomy for hydrocephalus treatment via a multicompartmental poroelastic model of CSF transport: A computational perspective. *PloS one, 8*, E84577.

Vermeer, P. A., & Verruijt, A. (1981). An accuracy condition for consolidation by finite elements. *International Journal for Numerical and Analytical Methods in Geomechanics, 5*, 1–14.

Vindedal, G. F., Thoren, A. E., Jensen, V., Klungland, A., Zhang, Y., Holtzman, M. J., … Nagelhus, E. A. (2016). Removal of aquaporin-4 from glial and ependymal membrane causes brain water accumulation. *Molecular and Cellular Neuroscience, 77*, 47–52.

Wang, H. F. (2000). *Theory of linear poroelasticity with applications to geomechanics and hydrogeology*. Princeton University Press.

Wang, S.-J., & Hsu, K.-C. (2009). The application of the first-order second-moment method to analyze poroelastic problems in heterogeneous porous media. *Journal of Hydrology, 369*, 209–221.

Wardlaw, J. M., Hernández, M. C. V., & Muñoz-Maniega, S. (2015). What are white matter hyperintensities made of? Relevance to vascular cognitive impairment. *Journal of the American Heart Association, 4*, E001140.

Wheeler, M. F., & Gai, X. (2007). Iteratively coupled mixed and Galerkin finite element methods for poro-elasticity. *Numerical Methods for Partial Differential Equations, 23*(4), 785–797.

Wilde, E., Aubdool, A. A., Thakore, P., Baldissera, L., Alawi, K. M., Keeble, J., … Brain, S. D. (2017). Tail-cuff technique and its influence on central blood pressure in the mouse. *Journal of the American Heart Association, 6*, E005204.

Wilson, R. K., & Aifantis, E. C. (1982). On the theory of consolidation with double porosity. *International Journal of Engineering Science, 20*(9), 1009–1035.

Winslow, R. L., Trayanova, N., Geman, D., & Miller, M. I. (2012). Computational medicine: Translating models to clinic care. *Science Translational Medicine, 4* 158rv11158rv11.

Wirth, B., & Sobey, I. (2006). An axisymmetric and fully 3D poroelastic model for the evolution of hydrocephalus. *Mathematical Medicine and Biology, 23*, 363–388.

Xie, L., Kang, H., Xu, Q., Chen, M. J., Liao, Y., Thiyagarajan, M., … Nedergaard, M. (2013). Sleep drives metabolite clearance from the adult brain. *Science (New York, N.Y.), 342*, 373–377.

Yamashita, K., Kobayashi, S., Yamaguchi, S., Kitani, M., & Tsunematsu, T. (1988). Effect of smoking on regional cerebral blood flow in the normal aged volunteers. *Gerontology, 34*, 199–204.

Yi, S.-Y. (2017). A study of two modes of locking in poroelasticity. *SIAM Journal of Numerical Analysis, 55*(4), 1915–1936.

Zienkiewicz, O. C., Chan, A. H. C., Pastor, M., Paul, D. K., & Shiomi, T. (1990). Static and dynamic behaviour of soils: A rational approach to quantitative solutions. I. Fully saturated problems. *Proceedings of the Royal Society of London A, 429*, 285–309.

Zienkiewicz, O. C., & Shiomi, T. (1984). Dynamic behaviour of saturated porous media; the generalized Biot formulation and its numerical solution. *International Journal for Numerical and Analytical Methods in Geomechanics, 8*, 71–96.